UNIVERSITÀ DEGLI STUDI DI PADOVA

DIPARTIMENTO DI SCIENZE CHIMICHE

CORSO DI LAUREA MAGISTRALE IN CHIMICA

TESI DI LAUREA MAGISTRALE

Signatures of Conical Intersections in Two-dimensional Electronic Spectra of Red-absorbing Squaraine Dyes

Relatore: Prof.ssa Elisabetta Collini
Controrelatore: Prof. Alessandro Soncini

Laureanda: Vittoria Burigana

Anno Accademico 2023/2024

Contents

Abstract

In recent years, squaraine dyes have garnered significant attention for their role in solution-processed photovoltaics due to their strong absorption in the red and near-infrared (NIR) region of the solar spectrum, which is not effectively harnessed by current technologies. Despite extensive experimental work and proposed applications, understanding the complex photophysics of these organic molecules, particularly in the ultrafast regime, remains limited.

This Thesis aims to provide a deeper understanding of the static and time-resolved photophysical properties of three commercially available squaraines: 2,4-bis[4-(N,N-diisobutylamino)-2,6-dihydroxyphenyl] squaraine(SQ), 2,4-bis[4-(N,N-diphenylamino)-2,6-dihydroxyphenyl] squaraine (DPSQ), 2,4-bis[4-(N,N-dibenzylamino)-2,6-dihydroxyphenyl] squaraine (DBSQ).

A combination of linear and nonlinear, static, and time-resolved optical spectroscopies was employed to investigate the origin of nonradiative decay pathways that might negatively affect the efficiency of these dyes as sensitizers for solar cells.

In particular, we focused on the results obtained by applying two-dimensional electronic spectroscopy (2DES), which has proven to be well-suited for studying the ultrafast dynamics of squaraine dyes. This technique enabled the detailed examination of processes occurring on the femtosecond timescale and facilitated the determination of the time constants associated with various relaxation pathways in squaraine solutions. The obtained experimental results revealed the presence of a conical intersection (CI) between the ground and the excited state, as highlighted by distinct spectral signatures that could be explained by a two-state two-mode model. The crucial role of at least two vibrational modes strongly coupled with the electronic degrees of freedom has been elucidated. The passage through a CI was identified as a crucial relaxation pathway for the excited state, shedding light on one of the factors contributing to the complexity of the photophysical behavior of these dyes.

List of Abbreviations

2DES	Two-dimensional electronic spectroscopy
2S2M	Two-state two-mode
A	Acceptor
AOPDF	Acousto-Optic Programmable Dispersive Filter
AcCN	Acetonitrile
BO	Born-Oppenheimer
CAS	Coherence associated spectra
CCD	Charge-coupled device
CI	Conical intersection
D	Donor
DAS	Decay associated spectra
DBSQ	2,4-bis[4-(N,N-dibenzylamino)-2,6-dihydroxyphenyl] squaraine
DHO	Displaced harmonic oscillator
DOE	Diffractive optic element
DPSC	2,4-bis[4-(N,N-diphenylamino)-2,6-dihydroxyphenyl] squaraine
DSM	Donut-shaped spherical mirror
DSSC	Dye-sensitized solar cell
ED	Excitonic dimer
ESA	Excited state absorption
EtOH	Ethanol
FC	Franck-Condon
FROG	Frequency resolved optical gating
FSC	Fourier spectrum of coherences
FT	Fourier transform
FWHM	Full width half maximum
FWM	Four-wave-mixing
GSB	Ground state bleaching
ICT	Intramolecular charge transfer
JC	Jaynes-Cummings
LO	Local oscillator
MeOH	Methanol
NIR	Near-infrared
NR	Non-rephasing
PES	Potential energy surface
R	Rephasing
sCMOS	Scientific Complementary Metal-Oxide Semiconductor
SE	Stimulated emission
SHG	Second harmonic generation
SQ	2,4-bis[4-(N,N-diisobutylamino)-2,6- dihydroxyphenyl] squaraine

TCSPC	Time-correlated single-photon counting
TFT	Time-frequency transform
TL	Transform-limited
T	Total
WP	Wavepacket

Introduction

The shortage of energy and the harmful environmental impact of fossil fuel consumption are among the most pressing issues faced by humanity today [1]. The development of alternative and renewable sources is essential not only to ensure a reliable energy supply but also to mitigate carbon dioxide emissions and other pollutants released during fossil fuel combustion. Solar energy, a highly promising renewable resource, provides approximately 6000 times more energy to Earth's surface than the world's current energy demand [2]. Photovoltaic technologies, such as dye-sensitized solar cells (DSSCs), offer a viable approach to harness this abundant energy. DSSCs, initially pioneered by Grätzel in 1991 [3], have attracted attention due to their low production costs, adaptability to low-light conditions, rapid energy payback, and ease of waste management [4]. These thin-film solar cells mimic the natural photosynthetic process by using dyes to absorb sunlight, producing excited electrons that are then injected into a semiconductor. The resulting current flows through an external circuit before being collected back by an electrolyte at the cathode, thus completing the cycle [5].

Compared to traditional silicon solar cells, DSSCs offer several advantages, particularly in applications requiring lightweight and flexible devices. To move away from traditional metal-based sensitizers, particularly Ru(II) complexes, and to address some of their inherent limitations, such as high costs and limited availability, researchers are exploring metal-free alternatives. These alternatives offer advantages, including higher absorption extinction coefficients and the potential for photon harvesting beyond the visible spectrum, extending into the red and near-infrared (NIR) wavelength regions, which accounts for more than half of the solar energy that reaches the Earth's surface. [6]. However, DSSCs with metal-free dyes generally exhibit lower energy conversion efficiencies, primarily due to their narrower absorption range in the solar spectrum [4]. Squaraine dyes have emerged as promising candidates for enhancing DSSCs performance, thanks to their strong absorption in the red and near-infrared (NIR) regions, straightforward synthesis routes, and high stability [7, 8, 9, 10]. Squaraines are squaric acid derivatives characterized by a donor-acceptor-donor (D-A-D) π-conjugated system, constituted by a central four-membered ring and two electron-donating groups. Since the early 2000s, several symmetrical and asymmetrical squaraine dyes have been studied as sensitizers in DSSCs. Despite extensive experimental work and various proposed applications, our understanding of their complex photophysics remains limited. Furthermore, it is unclear which specific properties regulate the efficiency of different squaraine dyes as photosensitizers in DSSCs, which hinders the design of new, more efficient molecular structures. To address this gap, this Thesis project aims to investigate the photophysical behavior of squaraine dyes with different molecular structures. The goal is to propose relationships between structure and properties. In particular, the attention was focused on the linear and nonlinear optical properties of three commercially available symmetrical red-absorbing squaraines. In particular, by exploring the ultrafast dynamics of these molecules we aim to gain important information about competitive nonradiative decay pathways undesired for solar cell efficiency, such as charge-recombination or thermal relaxation processes driven by vibronic coupling. Indeed, to maximize efficiency, DSSCs dyes must maintain charge separation long enough to facilitate effective electron injection into the

substrate [4]. Nonradiative decay pathways are therefore detrimental to the performance of the device, particularly in the case of red-absorbing dyes, due to their low energy transition.

A comprehensive understanding of the microscopic processes that influence DSSC efficiency can be achieved through time-resolved optical spectroscopy. In particular, two-dimensional electronic spectroscopy (2DES) is a powerful technique for probing the ultrafast dynamics of complex chromophoric systems and quantifying nonradiative contributions to their relaxation processes. 2DES has been widely used to study energy and charge transport mechanisms in biological and artificial light-harvesting systems, as well as their interactions with the environment and nuclear degrees of freedom [11, 12, 13]. The technique can be broadly classified as a four-wave-mixing heterodyne detected spectroscopy featuring ultrafast (<15 femtoseconds) temporal resolution. It utilizes a sequence of three ultrashort laser pulses to induce a third-order nonlinear optical response, which is represented in the form of 2D frequency-frequency correlation maps that evolve over time [14]. The presence of couplings, such as vibronic coupling, is indicated by the emergence of cross-peaks and enables the isolation and identification of vibronic contributions. The multidimensionality of this technique combined with its temporal resolution, provides 2DES with a significant advantage over conventional one-dimensional techniques, such as pump-probe spectroscopy, and makes 2DES particularly suitable for the objectives of this Thesis.

This Thesis is organized as follows:

- *Chapter 1* provides the theoretical background for describing nonlinear time-resolved optical spectroscopy, with a particular focus on the basis of 2DES. Additionally, it includes a brief introduction to conical intersections, to contextualize the experimental results.
- *Chapter 2* describes the systems under investigation, consisting of a selection of three symmetrical squaraines, along with their preliminary optical characterization using linear spectroscopies.
- *Chapter 3* details the optical setup used in the 2DES experiments and the analysis toolbox developed for data processing, analysis, and interpretation.
- *Chapter 4* presents the experimental results obtained through 2DES characterization and their interpretation.

1 Theoretical Background

To gain a deeper understanding of 2DES and the results presented in this work, it is essential to first address the underlying theory.
This chapter will begin by exploring the foundational concepts and quantum-mechanical tools underpinning 2DES, following the response function formalism [15]. Thereafter, a brief discussion of conical intersections (CIs) will be provided, as their role is crucial for interpreting the findings presented in the subsequent Sections.

1.1 Light-Matter Interaction

Spectroscopy is the study of the interaction between light and matter, allowing the exploration of both the electronic structure and dynamics of matter.

In this context, light and matter are treated as a single system that can be described through a Hamiltonian, specified as the sum of three terms:

$$\widehat{H} = \widehat{H}_M + \widehat{H}_L + \widehat{H}_{int} \tag{1.1}$$

where $\widehat{H}_M$ is the Hamiltonian of matter, $\widehat{H}_L$ represents the Hamiltonian of light and $\widehat{H}_{int}$ accounts for their mutual interaction.

To simplify the diagonalization of this Hamiltonian, it is convenient to apply the so-called *semi-classical* approximation, in which the light is described classically and the matter quantum-mechanically. This allows to neglect the $\widehat{H}_L$ term, such that Equation (1.1) becomes [16]:

$$\widehat{H} = \widehat{H}_M + \widehat{H}_{int} \tag{1.2}$$

In the semiclassical approximation, the light is described as a wave by using Maxwell's equations, leading to the wave equation of the electrical field, which in vacuum takes the form:

$$\widehat{\nabla}^2\mathbf{E}(\mathbf{r},t) - \frac{1}{c^2}\frac{\partial^2}{\partial t^2}\mathbf{E}(\mathbf{r},t) = 0 \tag{1.3}$$

and a possible general solution can be written as a plane wave [17]:

$$\mathbf{E}(\mathbf{r},t) = 2E_0(t)\widehat{\epsilon}cos(\mathbf{k}\cdot\mathbf{r}-\omega t) = E_0(t)\widehat{\epsilon}\left[e^{i(\mathbf{k}\cdot\mathbf{r}-\omega t)} + e^{-i(\mathbf{k}\cdot\mathbf{r}-\omega t)}\right] \tag{1.4}$$

This equation describes the electric field as a function that oscillates in time along a direction defined by the unitary vector $\widehat{\epsilon}$, amplitude E_0, and frequency ω and that propagates through space in the direction defined by the wavevector $\mathbf{k}$, with module $k = \frac{\omega}{c}$.

On the other hand, matter is treated as a distribution of charges, whose distribution is modified after the interaction with an external electric field. The macroscopic result of this process is called polarization [18], which can be generally expressed as a power expansion of $\mathbf{E}$:

$$\mathbf{P} = \epsilon_0[\chi^{(1)}\cdot\mathbf{E} + \chi^{(2)}\cdot\mathbf{E}^2 + \chi^{(3)}\cdot\mathbf{E}^3 + ...] = \mathbf{P}^{(1)} + \mathbf{P}^{(2)} + \mathbf{P}^{(3)} + ... \tag{1.5}$$

where $\chi^{(n)}$ is the nth order susceptibility, a tensor quantity, and ϵ_0 the dielectric permittivity in vacuum.

Under these conditions, the wave equation previously formulated in vacuum for **E**, Equation (1.3) is corrected for propagation in a medium as [19]:

$$\widehat{\nabla}^2\mathbf{E}(\mathbf{r},t) - \frac{1}{c^2}\frac{\partial^2\mathbf{E}(\mathbf{r},t)}{\partial t^2} = \frac{1}{\epsilon_0 c^2}\frac{\partial^2\mathbf{P}(\mathbf{r},t)}{\partial t^2} \tag{1.6}$$

The material's polarization $\mathbf{P}(t)$ is a crucial quantity in this discussion, being the primary physical observable of a spectroscopic experiment. Indeed, the signal emitted from the sample, $\mathfrak{S}$, is directly proportional to the polarization [20]:

$$\mathfrak{S} \propto iP(t) \tag{1.7}$$

For weak electric fields, the polarization can be adequately described only considering the linear term. However, when the light source is more intense, such as in the case of laser light, nonlinear terms become significant and cannot be neglected. Therefore, Equation (1.5) can be conveniently rewritten as:

$$\mathbf{P}(\mathbf{r},t) \equiv \mathbf{P}^{(1)}(\mathbf{r},t) + \mathbf{P}^{NL}(\mathbf{r},t) \tag{1.8}$$

In the upcoming sections, the significance of the quantity **P** will be extensively emphasized, as it is linked to the nonlinear response function *S*, presented in Section 1.4.

1.2 Time Evolution of the Wavefunction

So far, the provided description has been from a macroscopic perspective. To understand the underlying processes within the system, it is essential to adopt a microscopic viewpoint based on quantum mechanics.

A quantum system is described in terms of its wavefunction $|\Psi(t)\rangle$, and its time evolution is governed by the solutions of the time-dependent Schrödinger equation:

$$\frac{\partial}{\partial t}|\Psi(t)\rangle = -\frac{i}{\hbar}\widehat{H}\,|\Psi(t)\rangle \tag{1.9}$$

The system's temporal evolution can also be determined through the definition of the *time-evolution operator*, which for a time-independent Hamiltonian is formulated as:

$$\widehat{\mathcal{U}}(t,t_0) = e^{-\frac{i}{\hbar}\widehat{H}\cdot(t-t_0)} \tag{1.10}$$

This operator is used to propagate the wavefunction from time t_0 to time t as follows:

$$|\Psi(t)\rangle \equiv \widehat{\mathcal{U}}(t,t_0)\,|\Psi(t_0)\rangle \tag{1.11}$$

It is important to note that solving the Schrödinger equation is equivalent to solving the equa-

tion of motion of the time-evolution operator [21], as they convey the same information:

$$\frac{\partial}{\partial t}\widehat{\mathcal{U}}(t,t_0) = -\frac{i}{\hbar}\widehat{H}\widehat{\mathcal{U}}(t,t_0) \tag{1.12}$$

Integrating Equation (1.12) between t_0 and t is the first step towards deriving its solution:

$$\widehat{\mathcal{U}}(t,t_0) = 1 - \frac{i}{\hbar}\int_{t_0}^{t} d\tau \widehat{H}(\tau)\widehat{\mathcal{U}}(\tau,t_0) \tag{1.13}$$

since by definition $\widehat{\mathcal{U}}(t_0,t_0) = 1$. This equation can then be solved iteratively according to:

$$\begin{gathered}\widehat{\mathcal{U}}(t,t_0) = exp_+\left[-\tfrac{i}{\hbar}\int_{t_0}^{t} d\tau \widehat{H}(\tau)\right] \\ \equiv 1 + \sum_{n=1}^{\infty}\left(-\tfrac{i}{\hbar}\right)^n \int_{t_0}^{t} d\tau_n ... \int_{t_0}^{\tau_2} d\tau_1 \widehat{H}(\tau_n)...\widehat{H}(\tau_1)\end{gathered} \tag{1.14}$$

where exp_+ is a positive time-ordered exponential [21].

Equation (1.14) depicts the evolution of a quantum system subjected to a time-dependent perturbation over a specific time interval, considering all potential paths from the initial state to the final one, through any number of intermediate states. A crucial aspect of this expression is the time-ordering, which in this case is:

$$t_0 \to \tau_1 \to \tau_2 \to \tau_3 \to ... \to \tau_n \to t \tag{1.15}$$

Going back to the wavefunction, the time evolution of the system can be expressed as:

$$|\Psi(t)\rangle = |\Psi(t_0)\rangle + \sum_{n=1}^{\infty}\left(-\frac{i}{\hbar}\right)^n \int_{t_0}^{t} d\tau_n ... \int_{t_0}^{\tau_2} d\tau_1 H(\tau_n)...H(\tau_1)\,|\Psi(t_0)\rangle \tag{1.16}$$

where $|\Psi(t_0)\rangle$ is the wavefunction of the unperturbed system.

Typically, the interaction with the external electric field is considered weak compared to the internal fields of the molecule, making it appropriate to treat the former as a perturbation of the system's energy. Under these conditions, it is possible to describe the dynamics of the system in a simplified way by applying the time-dependent perturbation theory. According to this formalism, it is possible to write the Hamiltonian as:

$$\widehat{H}(t) = \widehat{H}_0(t) + \widehat{V}(t) \tag{1.17}$$

where $\widehat{H}_0(t)$ is the Hamiltonian of the unperturbed system, which is generally well known and defined, and $\widehat{V}(t)$ is the term accounting for a weak interaction, suitable for a perturbative treatment.

The interaction Hamiltonian $\widehat{V}(t)$ is typically expressed as a multipolar expansion:

$$\widehat{V}(t) = Q\phi - \widehat{\boldsymbol{\mu}}\cdot\mathbf{E} + ... \tag{1.18}$$

where Q is the net charge, ϕ is the electrostatic potential, $\widehat{\boldsymbol{\mu}}$ is the electric dipole moment and $\mathbf{E}$ is the electric field; the subsequent terms account for interactions between higher rank tensors. Considering a medium with no neat charge (Q=0) and truncating the expansion to the first non-zero term, justified by the inverse proportionality of the terms to powers of the distance, the Hamiltonian becomes [20]:

$$\widehat{H}(t) = \widehat{H}_0 - \widehat{\mu}E(t) \tag{1.19}$$

(where the vector nature of $\widehat{\boldsymbol{\mu}}$ has been neglected by assuming it to be parallel to the electric field). At this point, it is beneficial to switch from the *Schrödinger picture*, implicitly applied so far, to the *interaction picture* or *Dirac representation* [15]. In the Schrödinger picture, the time dependence is fully enclosed in the wavefunctions, while in the interaction picture, both wavefunctions and the operators carry time dependence. This approach is particularly useful when the system's Hamiltonian can be factorized as in Equation (1.17).

In the interaction picture, a new set of wavefunctions can be defined as:

$$|\Psi_S(t)\rangle \equiv \widehat{\mathcal{U}}_0(t,t_0)\,|\Psi_I(t)\rangle \tag{1.20}$$

where $|\Psi_S(t)\rangle$ is the wavefunction within the Schrödinger picture and $\widehat{\mathcal{U}}_0(t,t_0)$ is the time-evolution operator in respect to only $\widehat{H}_0$. Indeed this propagator can be introduced as the solution of Equation (1.12) for the unperturbed Hamiltonian:

$$\begin{gathered}\widehat{\mathcal{U}}_0(t,t_0) = exp_+\left[-\tfrac{i}{\hbar}\int_{t_0}^{t} d\tau \widehat{H}_0(\tau)\right] \\ \equiv 1 + \textstyle\sum_{n=1}^{\infty}\left(-\tfrac{i}{\hbar}\right)^n \int_{t_0}^{t} d\tau_n \int_{t_0}^{\tau} d\tau_{n-1} ... \int_{t_0}^{\tau_2} d\tau_1 \widehat{H}_0(\tau_n)\widehat{H}_0(\tau_{n-1})...\widehat{H}_0(\tau_1)\end{gathered} \tag{1.21}$$

Therefore, the time dependence of $|\Psi_I(t)\rangle$ describes the evolution of the wavefunction due to the difference between $\widehat{H}(t)$ and $\widehat{H}_0(t)$, thus is only related to the applied perturbation $\widehat{V}(t)$.

When replacing Equation (1.20) into Equation (1.9), the result is substantially equivalent to the Schrödinger equation:

$$\frac{d}{dt}\,|\Psi_I(t)\rangle = -\frac{i}{\hbar}\widehat{V}_I(t)\,|\Psi_I(t)\rangle \tag{1.22}$$

where the perturbation in the interaction picture is defined as:

$$\widehat{V}_I(t) = \widehat{\mathcal{U}}_0^{\dagger}(t,t_0)\widehat{V}(t)\widehat{\mathcal{U}}_0(t,t_0) = e^{\frac{i}{\hbar}\widehat{H}_0(t-t_0)}\widehat{V}(t)e^{-\frac{i}{\hbar}\widehat{H}_0(t-t_0)} \tag{1.23}$$

Analogously to the previous definition of $\widehat{\mathcal{U}}_0(t,t_0)$ it is possible to define also $\widehat{\mathcal{U}}_I(t,t_0)$, referred to the perturbation, as:

$$\begin{gathered}\widehat{\mathcal{U}}_I(t,t_0) = exp_+\left[-\tfrac{i}{\hbar}\int_{t_0}^{t} d\tau \widehat{V}_I(\tau)\right] \\ \equiv 1 + \textstyle\sum_{n=1}^{\infty}\left(-\tfrac{i}{\hbar}\right)^n \int_{t_0}^{t} d\tau_n \int_{t_0}^{\tau} d\tau_{n-1} ... \int_{t_0}^{\tau_2} d\tau_1 \widehat{V}_I(\tau_n)\widehat{V}_I(\tau_{n-1})...\widehat{V}_I(\tau_1)\end{gathered} \tag{1.24}$$

Analogously to what has been done before, Equation (1.22) can be solved using an iterative

procedure:

$$\begin{aligned} |\Psi_I(t)\rangle &= \widehat{\mathcal{U}}_I(t,t_0)\,|\Psi_I(t_0)\rangle \\ &= |\Psi_I(t)\rangle = |\Psi_I(t_0)\rangle \\ &+ \textstyle\sum_{n=1}^{\infty}\left(-\frac{i}{\hbar}\right)^n \int_{t_0}^{t} d\tau_n \int_{t_0}^{\tau_n} d\tau_{n-1} \ldots \int_{t_0}^{\tau_2} d\tau_1 \widehat{V}_I(\tau_n)\widehat{V}_I(\tau_{n-1})\ldots\widehat{V}_I(\tau_1)\,|\Psi_I(t_0)\rangle \end{aligned} \tag{1.25}$$

Focusing on each single term within the summation allows the reader to infer the physical meaning of this expression. The system is at equilibrium until time τ_1, at which the perturbation $\widehat{V}(\tau_1)$ is applied. After this, the system will propagate freely until time τ_2, when it interacts with the second perturbation $\widehat{V}(\tau_2)$, and so forth. This concept can be better understood through *Feynman diagrams*, an important graphical tool that will be presented in Section 1.4.2.

The formalism presented is well-suited for describing a *pure state*, which pertains to a system that can be represented by a single wavefunction. However, in the condensed phase, it becomes essential to consider statistical ensembles of quantum systems in various states, commonly referred to as *mixed states*. In such scenario, it is more appropriate to use the density operator $\widehat{\rho}(t)$, as discussed in the next Section.

1.3 Density Matrix Formalism

The density operator is defined as the outer product of the wavefunction and its complex conjugate [21]:

$$\widehat{\rho}(t) = |\Psi(t)\rangle\,\langle\Psi(t)| \tag{1.26}$$

This expression can be generalized considering a statistical ensemble made of different replicas of a quantum system, where each replica is associated with a probability p_k of being in the state $|\Psi_k\rangle$. In this case, $\widehat{\rho}(t)$ can be written as:

$$\widehat{\rho}(t) = \sum_k p_k\,|\Psi_k(t)\rangle\,\langle\Psi_k(t)| \tag{1.27}$$

In Equation (1.27), the values of p_k are non-negative and normalized. When all p_k are null except for one, which is equal to 1, the system is in a pure state, as previously explained.

The density operator can be conveniently represented as a matrix. Using an arbitrary basis set $|n\rangle$, the wavefunction and its complex conjugate can be written as:

$$\begin{aligned} |\Psi_k(t)\rangle &= \sum_n c_n^{(k)}(t)\,|n\rangle \\ \langle\Psi_k(t)| &= \sum_m c_m^{(k)*}(t)\,\langle m| \end{aligned} \tag{1.28}$$

where $c_n^{(k)}$ are the expansion coefficient and $c_m^{(k)*}$ their complex conjugate.

Therefore the matrix elements will be defined as [16]:

$$\rho_{nm}(t) = \langle n|\,\widehat{\rho}(t)\,|m\rangle = \sum_k p_k \langle n|\Psi_k(t)\rangle\langle\Psi_k(t)|m\rangle = \sum_k p_k c_n^{(k)}(t) c_m^{(k)*}(t) \tag{1.29}$$

The diagonal elements $(n = m)$ are called *populations* and represent the probability of the system of being in the n^{th} eigenstate:

$$\rho_{nn} = \overline{c_n c_n^*} = p_n \tag{1.30}$$

where the overline denotes averaging over the statistical ensemble.
The off-diagonal elements $(n \neq m)$ are complex quantities and are defined as *coherences*. These represent coherent superpositions of states that oscillate with a specific frequency ω_{mn}:

$$\rho_{nm} = \overline{c_n(t)c_m^*(t)} = \overline{c_n c_m^*} e^{-i\omega_{mn}t} \tag{1.31}$$

with $\omega_{mn} = \omega_m - \omega_n = (E_m - E_n)/\hbar$, where E_n and E_m are the energies of the states involved in the superposition.

The use of the density operator provides significant advantages. This becomes evident when calculating the expectation value of a generic operator $\widehat{A}$:

$$\begin{aligned} \langle\widehat{A}(t)\rangle &= \langle\Psi(t)|\,\widehat{A}\,|\Psi(t)\rangle = \textstyle\sum_{n,m} c_n(t)c_m^*(t)\,\langle m|\,\widehat{A}\,|n\rangle \\ &= \textstyle\sum_{n,m} A_{mn}\rho_{nm}(t) = Tr\,[A\rho(t)] \end{aligned} \tag{1.32}$$

as the problem is simplified by moving the complexity of the calculation from an integral to a trace of a product of matrices.

In the previous Section, the time evolution of a pure state was investigated. Similarly, it can be done for mixed states using the equation of motion of $\widehat{\rho}$:

$$\frac{\partial}{\partial t}\widehat{\rho}(t) = -\frac{i}{\hbar}[\widehat{H}(t), \widehat{\rho}(t)] \tag{1.33}$$

known as the Liouville-von Neumann equation, which is the equivalent of the Schrödinger equation in the frame of the density matrix formalism.

Within the interaction picture, Equation (1.33) can be rewritten as:

$$\frac{\partial}{\partial t}\widehat{\rho}_I(t) = -\frac{i}{\hbar}[\widehat{V}_I(t), \widehat{\rho}_I(t)] \tag{1.34}$$

aknowledging that the density operator $\widehat{\rho}_I(t)$ is defined as:

$$\widehat{\rho}(t) = \widehat{\mathcal{U}}_0(t, t_0)\widehat{\rho}_I(t)\widehat{\mathcal{U}}_0^\dagger(t, t_0) \tag{1.35}$$

Also in this case, it is possible to solve Equation (1.34) by applying an iterative procedure:

$$\widehat{\rho}_I(t) = \widehat{\rho}_I(t_0)$$

$$+\sum_{n=1}^{\infty}\left(-\tfrac{i}{\hbar}\right)^n \int_{t_0}^{t} d\tau_n ... \int_{t_0}^{\tau_2} d\tau_1 \left[\widehat{V}_I(\tau_n), \left[\widehat{V}_I(\tau_{n-1}), ..., \left[\widehat{V}_I(\tau_1), \widehat{\rho}_I(t_0)\right]\right]\right] \tag{1.36}$$

$$= \widehat{\rho}_I(t_0) + \sum_{n=1}^{\infty} \widehat{\rho}_I^{(n)}(t)$$

where

$$\widehat{\rho}_I^{(n)}(t) = \left(-\frac{i}{\hbar}\right)^n \int_{t_0}^{t} d\tau_n ... \int_{t_0}^{\tau_2} d\tau_1 \left[\widehat{V}_I(\tau_n), \left[\widehat{V}_I(\tau_{n-1}), ..., \left[\widehat{V}_I(\tau_1), \widehat{\rho}_I(t_0)\right]\right]\right] \tag{1.37}$$

In this way, the perturbative expansion for the density operator was obtained [15]. This expression holds significant value within the context of nonlinear spectroscopy [21], as it will be later elaborated in Section 1.4.

1.4 Response Theory

The response theory serves as the primary tool for describing the evolution of a system away from thermal equilibrium, under perturbative conditions. It is particularly attractive as it connects measurable quantities obtained from spectroscopic measurements to microscopic quantum-mechanical properties.

Based on the perturbative approximation, it is possible to describe the expectation value of a generic operator $\widehat{A}$ as:

$$\langle \widehat{A}(t) \rangle = \langle \widehat{A}(-\infty) \rangle + \delta\overline{A(t)} = \langle \widehat{A}(-\infty) \rangle + \int_{-\infty}^{t} dt_0 S(t, t_0) f(t_0) + ... \tag{1.38}$$

where $\langle \widehat{A}(-\infty) \rangle$ is the equilibrium value before the perturbation, t_0 is the time at which the external stimulus $f(t_0)$ is applied and t is the observation time. $S(t, t_0)$ accounts for the *response* of the system that is enclosed in an integral that extends over the 'time history' of the system's perturbation.

This formalism can be employed to describe the polarization **P**(t), a key quantity for spectroscopy, as previously emphasized. Indeed, **P**(t) can also be defined as the average value of the dipole operator $\widehat{\boldsymbol{\mu}}$. By utilizing the density operator formalism, it is viable to restate the polarization expression as [15, 20]:

$$\mathbf{P}(t) = Tr[\widehat{\boldsymbol{\mu}} \cdot \widehat{\rho}(t)] \tag{1.39}$$

This expression can be generalized for the n^{th}-order within the interaction picture:

$$\mathbf{P}^{(n)}(t) = Tr[\widehat{\boldsymbol{\mu}}_I \cdot \widehat{\rho}_I^{(n)}(t)] \tag{1.40}$$

Now, by substituting Equation (1.37) into Equation (1.39), remembering that $\widehat{V}_I(t) = -\widehat{\boldsymbol{\mu}}_I \cdot \mathbf{E}(t)$:

$$\mathbf{P}^{(n)}(t) = \left(-\frac{i}{\hbar}\right)^n \int_0^\infty dt_n \int_0^\infty dt_{n-1} ... \int_0^\infty dt_1 \mathbf{E}(t-t_n) \cdot \mathbf{E}(t-t_n-t_{n-1}) \cdot ... \\ \cdot \mathbf{E}(t-t_n-t_{n-1}-...-t_1) \\ \cdot Tr\left\{\widehat{\boldsymbol{\mu}}_I(t_n+t_{n-1}+...+t_1)\left[\widehat{\boldsymbol{\mu}}_I(t_{n-1}+...+t_1), ...\left[\widehat{\boldsymbol{\mu}}_I(0), \widehat{\rho}_I(t_0)\right]\right]\right\} \quad (1.41)$$

where a new set of variables was defined as:

$$\tau_n = t - t_n$$
$$\tau_{n-1} = t - t_n - t_{n-1}$$
$$...$$

The time definitions are represented in Figure (1.1), where the time-zero point is arbitrarily set to $\tau_1 = 0$, when the first perturbation is applied to the system.

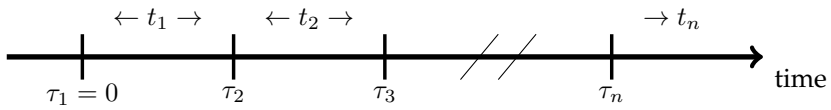

Figure 1.1: Time ordering in the definition of the n^{th}-order polarization. The time variables t_n indicate the time intervals while τ_n are referred to absolute time points.

By comparison with the first-order term of Equation (1.38), Equation (1.41) may also be expressed more simply as:

$$\mathbf{P}^{(n)}(t) = \int_0^\infty dt_n \int_0^\infty dt_{n-1} ... \int_0^\infty dt_1 \mathbf{E}(t-t_n) \\ \cdot \mathbf{E}(t-t_n-t_{n-1}) \cdot ... \cdot \mathbf{E}(t-t_n-...-t_1) \cdot S^{(n)}(t_n, t_{n-1}, ..., t_1) \quad (1.42)$$

where the external stimuli, previously generically indicated with f, now explicitly refer to the applied electric field.

Finally, it is possible to obtain the expression for the response function $S^{(n)}(t_n, ...t_1)$ [15]:

$$S^{(n)}(t_n, ...t_1) = \left(-\frac{i}{\hbar}\right)^n Tr\left\{\widehat{\boldsymbol{\mu}}_I(t_n+...t_1)\left[\widehat{\boldsymbol{\mu}}_I(t_{n-1}+...+t_1), ...\left[\widehat{\boldsymbol{\mu}}_I(0), \widehat{\rho}_I(t_0)\right]\right]\right\} \quad (1.43)$$

where $\widehat{\rho}_I(t_0)$ is the density operator at the equilibrium, also reported as $\widehat{\rho}_{eq}$.
Note that the response function $S^{(n)}$ is a real quantity directly connected to the observable.

1.4.1 Third Order Response Function

The third-order response function is of particular interest: it represents the lowest order permitting the investigation of excited states properties and offers the justification for the optical signal of

nonlinear techniques that employ excitation with three laser pulses, such as 2DES [20, 22].

According to the treatment outlined in the preceding Sections, the third-order polarization is expressed as:

$$\mathbf{P}^{(3)}(t) = \int_0^\infty dt_3 \int_0^\infty dt_2 \int_0^\infty dt_1 \mathbf{E}(t-t_3)\mathbf{E}(t-t_3-t_2)\mathbf{E}(t-t_3-t_2-t_1)S^{(3)}(t_3,t_2,t_1) \tag{1.44}$$

where the third-order response function is:

$$S^{(3)}(t_3,t_2,t_1) = \left(-\frac{i}{\hbar}\right)^3 Tr\left\{\widehat{\boldsymbol{\mu}}_I(t_3+t_2+t_1)[\widehat{\boldsymbol{\mu}}_I(t_3+t_2),[\widehat{\boldsymbol{\mu}}_I(t_1),[\widehat{\boldsymbol{\mu}}_I(0),\widehat{\rho}_{eq}]]]\right\} \tag{1.45}$$

This expression can be rewritten in a more convenient way by explicitly calculating the commutators:

$$S^{(3)}(t_3,t_2,t_1) = \left(-\frac{i}{\hbar}\right)^3 \sum_{\alpha=1}^{4} [R_\alpha(t_3,t_2,t_1) - R_\alpha^*(t_3,t_2,t_1)] \tag{1.46}$$

R_α (and their associated complex conjugates R_α^*) represent the so-called *Liouville pathways*. For the third-order treatment, $2^3 = 8$ pathways are generated, each one described as a trace of a product of matrices, as explicitly shown in Equation (1.47) [15].

$$\begin{aligned}
R_1(t_3,t_2,t_1) &= Tr\,[\widehat{\boldsymbol{\mu}}_I(t_1+t_2+t_3)\widehat{\boldsymbol{\mu}}_I(t_1+t_2)\widehat{\boldsymbol{\mu}}_I(t_1)\widehat{\boldsymbol{\mu}}(0)\widehat{\rho}_{eq}] \\
R_1^*(t_3,t_2,t_1) &= Tr\,[\widehat{\boldsymbol{\mu}}_I(t_1+t_2+t_3)\widehat{\rho}_{eq}\widehat{\boldsymbol{\mu}}(0)\widehat{\boldsymbol{\mu}}_I(t_1)\widehat{\boldsymbol{\mu}}_I(t_1+t_2)] \\
R_2(t_3,t_2,t_1) &= Tr\,[\widehat{\boldsymbol{\mu}}_I(t_1+t_2+t_3)\widehat{\boldsymbol{\mu}}_I(t_1)\widehat{\rho}_{eq}\widehat{\boldsymbol{\mu}}(0)\widehat{\boldsymbol{\mu}}_I(t_1+t_2)] \\
R_2^*(t_3,t_2,t_1) &= Tr\,[\widehat{\boldsymbol{\mu}}_I(t_1+t_2+t_3)\widehat{\boldsymbol{\mu}}_I(t_1+t_2)\widehat{\boldsymbol{\mu}}(0)\widehat{\rho}_{eq}\widehat{\boldsymbol{\mu}}_I(t_1)] \\
R_3(t_3,t_2,t_1) &= Tr\,[\widehat{\boldsymbol{\mu}}_I(t_1+t_2+t_3)\widehat{\boldsymbol{\mu}}_I(t_1+t_2)\widehat{\rho}_{eq}\widehat{\boldsymbol{\mu}}(0)\widehat{\boldsymbol{\mu}}_I(t_1)] \\
R_3^*(t_3,t_2,t_1) &= Tr\,[\widehat{\boldsymbol{\mu}}_I(t_1+t_2+t_3)\widehat{\boldsymbol{\mu}}_I(t_1)\widehat{\boldsymbol{\mu}}(0)\widehat{\rho}_{eq}\widehat{\boldsymbol{\mu}}_I(t_1+t_2)] \\
R_4(t_3,t_2,t_1) &= Tr\,[\widehat{\boldsymbol{\mu}}_I(t_1+t_2+t_3)\widehat{\boldsymbol{\mu}}(0)\widehat{\rho}_{eq}\widehat{\boldsymbol{\mu}}_I(t_1)\widehat{\boldsymbol{\mu}}_I(t_1+t_2)] \\
R_4^*(t_3,t_2,t_1) &= Tr\,[\widehat{\boldsymbol{\mu}}_I(t_1+t_2+t_3)\widehat{\boldsymbol{\mu}}_I(t_1+t_2)\widehat{\boldsymbol{\mu}}_I(t_1)\widehat{\rho}_{eq}\widehat{\boldsymbol{\mu}}(0)]
\end{aligned} \tag{1.47}$$

Each Liouville pathway accounts for a distinct sequence of light-matter interactions involving the three exciting fields, resulting in a specific density matrix evolution. The assignment of physical meaning to each path is nontrivial, thus diagrammatic methods, such as double-sided *Feynman diagrams* are widely employed.

1.4.2 Double-sided Feynman diagrams

As illustrated in Figure (1.2), these diagrams can be constructed by following a precise set of rules:

i. The time evolution of the *ket* and the *bra* of the density operator is depicted by vertical lines,

respectively on the left and right sides. Time progresses from the bottom to the top of the diagram.

ii. Arrows represent interactions with the electric field: interactions with a positive frequency (negative frequency) field are represented by arrows pointing to the left (right).

iii. The final arrow, typically indicated with a wavy line, represents the emission of the signal from the sample. As a convention, it is drawn on the left side of the diagram (or on the right side in the case of the conjugate complex).

iv. Absorption interactions are depicted with arrows pointing toward the system, while emission interactions are shown with arrows pointing away from it.

v. Before the first interaction, the system is in equilibrium, usually in the ground state. After the emission of the signal, the system returns to a population state, either ground ($|g\rangle\langle g|$) or excited ($|e\rangle\langle e|$).

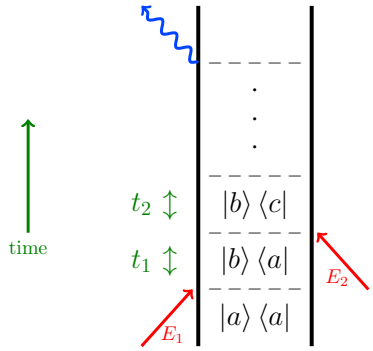

Figure 1.2: General example of a double-sided Feynman diagram for a multilevel system. The external electric fields are depicted in red, while the time evolution of the system is shown in green. The diagram illustrates the sequence of interactions and the transitions between different states $a, b, c, ...$, highlighting the coherent dynamics and population evolution throughout the process. The states $a, b, c, ...$ are arbitrary states for illustrative purposes.

As shown in Equation (1.46), only four terms are required for the third-order response function. The corresponding double-sided Feynman diagrams are illustrated in Figure (1.3), specifically for a two-level system. R_1 and R_3 are the pathways associated with the ground state bleaching (GSB) process: the first two pulses reduce the ground state population and the third generates a coherence between the ground and the excited states, responsible for the emission of the signal. On the other hand, R_2 and R_4 refer to the stimulated emission (SE) process, where the first two pulses lead to the excited state, and the third induces the coherence that ultimately generates the signal.

The emitted signal has a wavevector $\mathbf{k}_{sig}$, which is derived as the combination of the wavevectors of the incident beams:

$$\mathbf{k}_{sig} = \sum_{n=1}^{3} \pm \mathbf{k}_n \tag{1.48}$$

This implies that it is possible to distinguish the signals originating from different Liouville pathways based on their wavevector, by selecting an appropriate experimental setup geometry. This separation of the total signal enables the isolation of the *rephasing* (R) and *non-rephasing* (NR) components:

$$\begin{aligned} \mathbf{k}_{sig}^{R} &= -\mathbf{k}_1 + \mathbf{k}_2 + \mathbf{k}_3 \\ \mathbf{k}_{sig}^{NR} &= +\mathbf{k}_1 - \mathbf{k}_2 + \mathbf{k}_3 \end{aligned} \tag{1.49}$$

The distinction between these two terms arises from their differing behavior during the t_1 and t_3 time intervals. For the rephasing component, the signal's phase evolves at conjugate frequencies during these intervals, resulting in an echo signal. In contrast, for the non-rephasing pathway, the phase evolves at the same frequency, and no echo is produced [21].

Thus, the specific terminology used for the time intervals between consecutive interactions is also clarified. The interval t_1 is referred to as *coherence time*, as the system is in a coherent superposition of ground and excited states following the first interaction. The interval t_2 is known as *population time* since the system can evolve in a pure state during this period. Finally, t_3 is called *rephasing time*, which is the time required to emit the signals.

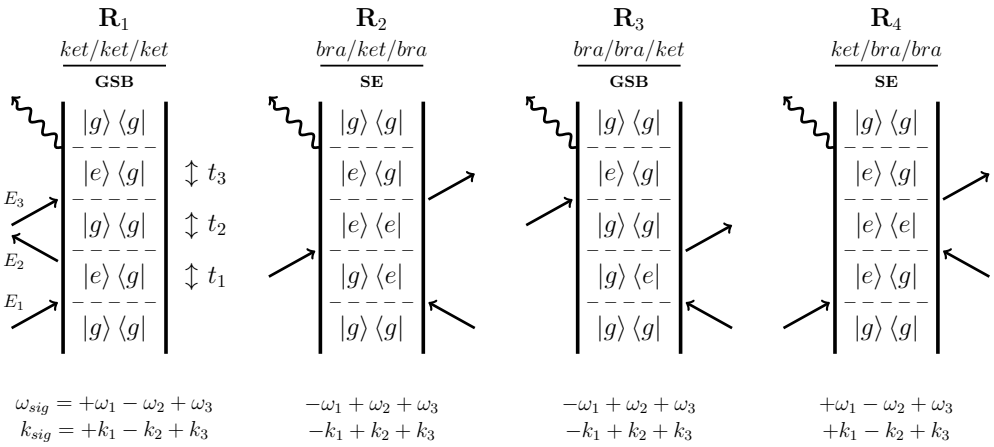

Figure 1.3: Feynman diagrams representing the third-order response function for a two-level system. The diagrams illustrate four different pathways: R_1 and R_3 correspond to GSB processes, while R_2 and R_4 represent SE processes. The signal wavevector for each pathway is indicated, with R_1 and R_4 contributing to the non-rephasing signal, and R_2 and R_3 contributing to the rephasing signal. The complex conjugate diagrams, R_α^*, are the mirror images of the ones shown and are therefore omitted for brevity.

Real systems are more complex than the simplified two-level model described above, requiring consideration of additional contributions to the signal. For example, if higher excited states are accessible, the third interaction may lead to absorption from the excited state: these pathways are referred to as excited state absorption (ESA). As reported in Figure (1.4), ESA pathways contribute to both rephasing and non-rephasing phase-matching conditions, and the corresponding signal always exhibits negative values. In contrast, GSB and SE pathways generate positive signals.

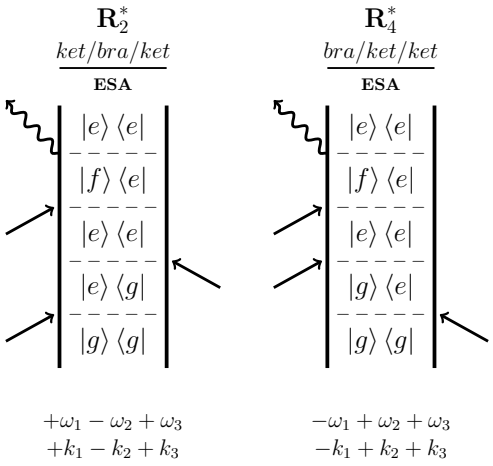

Figure 1.4: Feynman diagrams illustrating the ESA pathways contributing to the third-order response function of a three-level system (with g ground state and e and f excited state; $E_e < E_f$). R_2^* contributes to non-rephasing signal while R_4^* to the rephasing component.

1.5 Two-dimensional Electronic Spectroscopy

Within the perturbative framework, 2DES can be categorized as a four-wave-mixing (FWM) technique. In FWM methods, the sample is illuminated by a sequence of three light pulses, and the fourth wave corresponds to the emitted signal, as depicted in Figure (1.5).

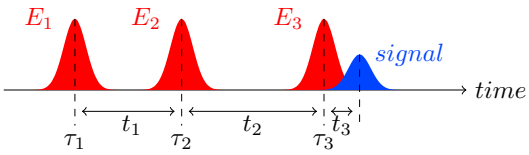

Figure 1.5: Pulse sequence in a two-dimensional electronic spectroscopy experiment.

The signal $\mathfrak{S}$ is therefore described by using the third-order response function $S^{(3)}(t_3, t_2, t_1)$ [14], as explained through Equations (1.7) and (1.44). Since interpreting the signal directly in the time domain would be extremely complicated, a Fourier transform (FT) is applied to t_1 and t_3 to simplify the visualization:

$$\mathfrak{S}(\omega_3, t_2, \omega_1) = \int_0^\infty \int_0^\infty dt_1 dt_3 \mathfrak{S}(t_3, t_2, t_1) e^{i\omega_3 t_3} e^{\pm i\omega_1 t_1} \tag{1.50}$$

where $\omega_1 = FT(t_1)$ and $\omega_3 = FT(t_3)$ are defined as excitation and detection frequency, respectively; the $\pm$ sign distinguishes between R and NR pathways.

As a result, the signal is represented in two-dimensional frequency-frequency maps, evolving over t_2. In these spectra, the x-axis corresponds to ω_1 and the y-axis to ω_3, as shown in Figure (1.6).

The multidimensionality of 2DES enables the exploration of various details related to the elec-

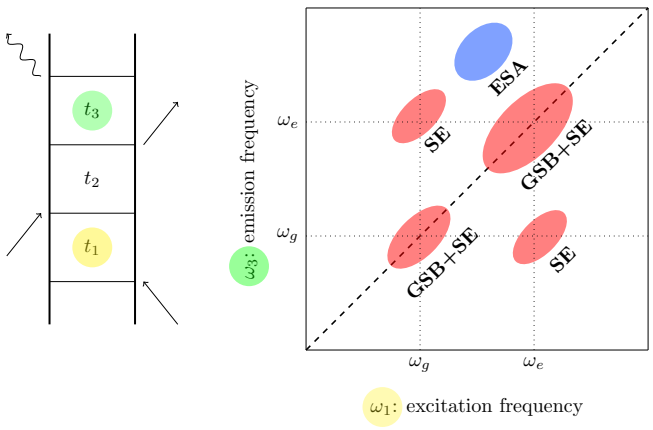

Figure 1.6: Typical structure of a 2D frequency-frequency map for a given t_2 value, where ω_1 and ω_3 are FTs of t_1 and t_3, respectively; the intensity of the signals appears in the maps with a color scale: red peaks are positive (GSB+SE) and blue ones are negative (ESA).

tronic structure, vibrational and electronic motions, interactions, couplings, and relaxation processes [22]. To extract all this information, two primary aspects must be analyzed: the peaks' position in the 2D map and their evolution over t_2.

About the peaks' position, two types of contributions to the signal can be distinguished:

i. **Diagonal peaks**, where the excitation and detection frequencies are the same, provide information on the frequencies of the main transitions involved in the studied photophysics. Therefore, the distribution of the signal along the diagonal reflects the energy landscape of the studied molecular system.

ii. On the other hand, **off-diagonal peaks** arise only in the presence of couplings between transitions or states (for example, in the presence of excitonic coupling, vibronic coupling, energy or charge transfer, etc.). The positions of these cross-peaks help identify which states are coupled. The presence (or absence) of these peaks in a 2D map provides insight into the nature of the electronic system. This capability extends to dynamic processes involving dark states, which can be identified through the appearance of ESA cross-peaks. Dark states may be populated through relaxation from higher-energy bright states, and once populated, they can absorb further into higher-excited states [22].

Regarding the system's evolution during t_2, two distinct types of contributions can be observed:

i. **Non-oscillating contributions** arise when, after the first two pulses, the system reaches a *population* state, as shown in Figure (1.7a). These dynamics can be described by solving appropriate kinetic differential equations.

ii. The second class, referred to as **oscillating contributions**, occurs when a coherent superposition of states is created after the first two pulses, as shown in Figure (1.7b), forming the

so-called *coherence* or *wavepacket* (WP) [23]. In agreement with the density matrix formalism (as discussed in Section 1.3), this signal oscillates along t_2 at a frequency proportional to the energy gap between the two states involved (see Equation (1.31)). These oscillations decay over time based on their dephasing rates, which depend on factors such as the nature of the states, temperature, and the environment [22], and are well described by complex exponential functions.

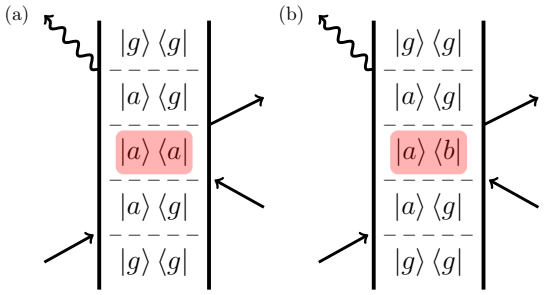

Figure 1.7: Examples of Feynman diagrams representing (a) non-oscillating and (b) oscillating contributions to the signal.

1.5.1 Electronic and Vibrational Coherences

So far, no assumptions have been made regarding the nature of the levels a and b involved in the coherent superposition evolving during t_2 in the beating diagrams (Figure (1.7b)). Indeed, they could be two different electronic states or two vibrational sub-levels belonging to the same electronic state. In the first case, we are discussing an electronic coherence that evolves over time, while in the second case, we are discussing a vibrational (or vibronic) coherence. Electronic and vibrational coherences can be both captured by 2DES and in many cases they can be distinguished by inspecting the signal distribution, as they generate distinct amplitude patterns in the 2D spectra [24]. These patterns can be accurately predicted using specific models, such as the excitonic dimer (ED) for electronic coherences and the displaced harmonic oscillator (DHO) for vibrational coherences.

Electronic coherences can be modeled using the ED approach [25]. This model describes two identical molecules (forming a homodimer), each having two levels consisting of an electronic ground state (g) and an excited state (e), without coupled vibrations. The molecules interact through an electrostatic coupling, characterized by the strength constant J. The resulting exciton dimer retains the same ground state as the monomers but forms new excitonic states, α and β. These are linear combinations of the monomer excited states, with opposite signs and energies equal to $\varepsilon_{\alpha,\beta} = \varepsilon \pm J$, where ε is the transition energy of the monomeric species. This three-level model, initially conceived for an excitonic homodimer, can describe any pair of coupled electronic states that can be simultaneously excited by the first two pulses.

Oscillating signals are thus generated by coherent superpositions of the excitonic states α and β. Both in rephasing and non-rephasing experiments, only two Feynman pathways contribute to these oscillating signals, as shown by the diagrams in Figure (1.8). These pathways produce two cross-peaks at coordinates (ε_α, ε_β) and (ε_β, ε_α) in the rephasing 2D map and two diagonal peaks at (ε_α, ε_α) and (ε_β, ε_β) in the non-rephasing 2D map. The signals oscillate at a frequency proportional to the energy difference between the two excitonic states, equal to $2J$.

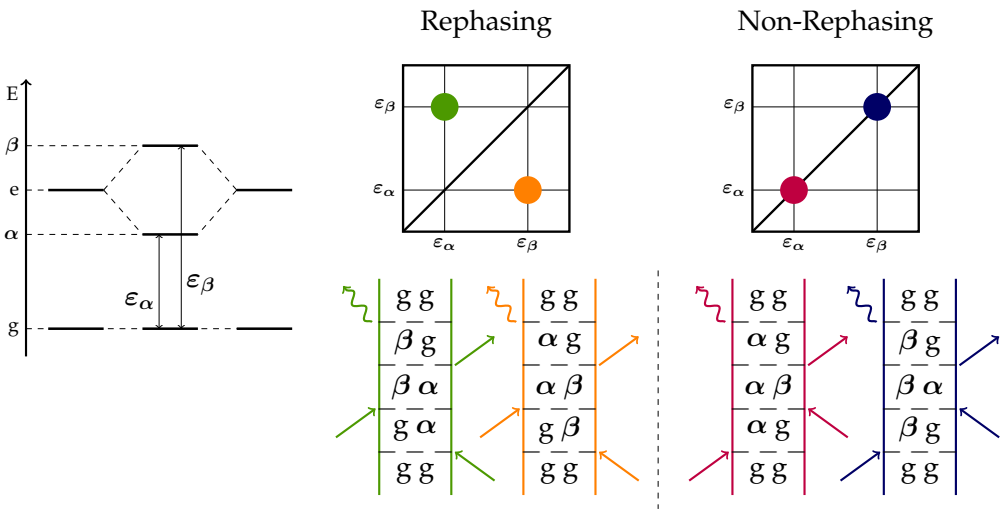

Figure 1.8: Excitonic dimer model illustrating the signatures of electronic coherences. The 2D maps for R and NR experiments are presented along with the corresponding Feynman diagrams. Each contribution is marked by a colored dot in the 2D maps, which correlates with the respective Feynman diagram of the same color.

Signals generated by Feynman pathways involving vibrational coherences during t_2 are commonly interpreted using a four-state model, known as the DHO model [24, 26], shown in Figure (1.9).

This model consists of two electronic states, the ground state (g) and an excited state (e), both coupled to a vibrational mode with frequency ω_{vib}. Under the assumption that the vibration is harmonic, the potential energy surfaces of the electronic states are represented by two parabolas: the excited state parabola is shifted upwards by the electronic transition energy ε and displaced along the nuclear coordinate.

The Feynman diagrams depict GSB and SE pathways, which produce oscillating signals during t_2. The frequencies of these oscillations can be either positive or negative, depending on the sign of the coherence during t_2. In the rephasing 2D maps, the peaks form a characteristic *chair-like* pattern, while in the non-rephasing 2D maps, this pattern is inverted.

The predictions from these two models suggest that it should be easy to differentiate between electronic and vibrational coherences by examining the beating distribution within the 2D maps.

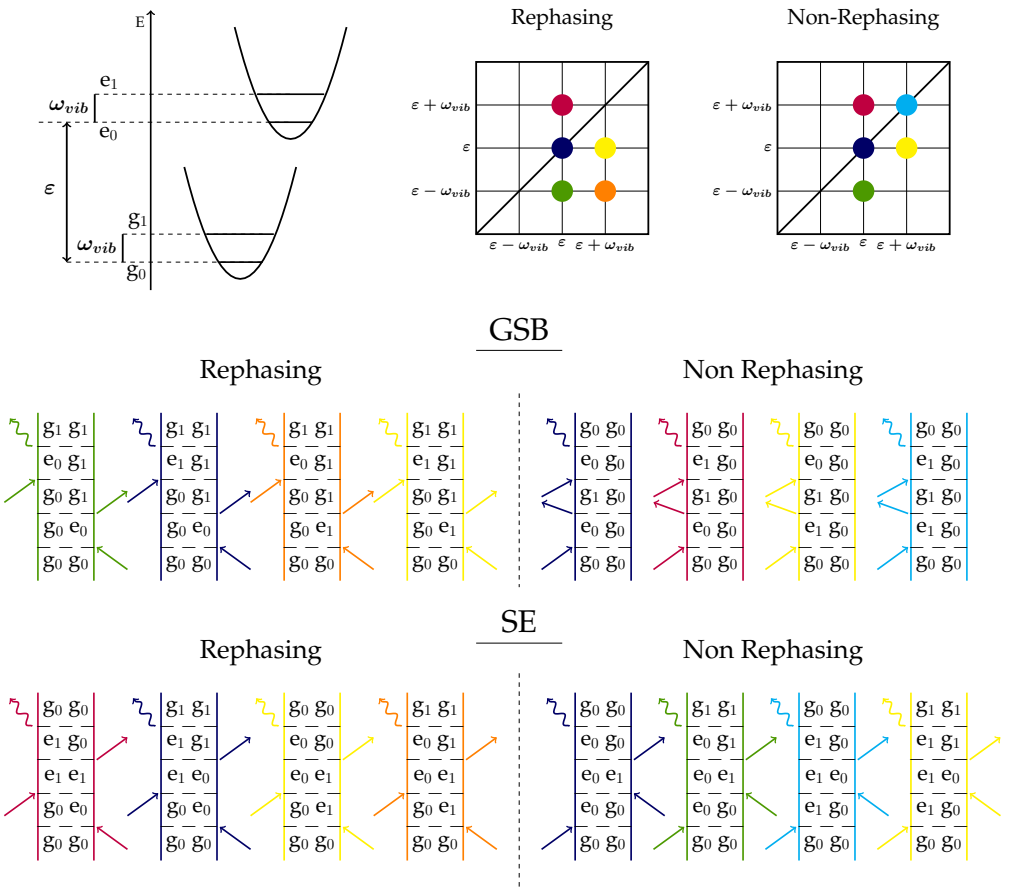

Figure 1.9: DHO model illustrating the signatures of vibrational coherences. The 2D maps for R (left) and NR (right) experiments are shown, along with the corresponding Feynman diagrams. Each contribution is represented by a colored dot in the 2D maps, corresponding to the Feynman diagram of the same color.

However, in real 2D map analysis, this task is not straightforward for several reasons. Firstly, excitonic coupling in aggregates often falls within the same energy range as vibrational modes, making pattern identification more complicated. Additionally, the DHO model neglects ESA contributions, which can be significant when higher-energy electronic states are involved, introducing new possible beating signals at different positions. Moreover, multiple vibrational modes may couple to a single electronic transition, resulting in additional oscillating signals at different coordinates in the spectrum [27]. This complexity necessitates careful signal analysis for accurate attributions and map interpretation. One approach to assist with this is to examine the dynamical behaviors: electronic coherences typically last for tens of femtoseconds at room temperature, while vibrational coherences can persist for up to a few picoseconds. Additionally, the comparison with other spectroscopic methods, such as IR or Raman spectroscopy—which are sensitive to vibrational modes—can help resolve the challenge.

1.6 2DES for Detecting Conical Intersections

With its capability to resolve signals both in time and frequency domains, 2DES is predicted to be particularly suitable for investigating complex ultrafast phenomena whose spectral signatures are often hidden in more conventional 1D spectroscopic responses. An example of these complex ultrafast phenomena is the presence of conical intersections (CIs) [28, 29].

1.6.1 Conical Intersections

As extensively discussed in previous Sections, the molecular behavior, including photoinduced dynamics, is described by the Schrödinger equation. To solve this complex equation, the Born-Oppenheimer (BO) approximation is commonly employed, allowing the separation of electronic and nuclear coordinates and the factorization of the wavefunction. This approach is justified by the significant mass difference between electrons and nuclei, which enables the assumption that their motions are independent [30]. The result is an approach known as the *adiabatic approximation*, where the Schrödinger equation is solved at fixed nuclear positions, yielding electronic energies as a function of these nuclear coordinates, thus forming potential energy surfaces (PESs). This approximation is sufficient to describe a wide range of phenomena and most chemical processes. However, in certain regions of the potential energy landscape, strong coupling between electronic and nuclear degrees of freedom causes the BO approximation to break down [31].
One prominent case in which the BO approximation fails is at CIs, defined as real crossing points between two electronic states [32, 33]. CIs are ubiquitous features in the photophysics and photochemistry of molecules [33, 34], and they are involved in processes as important as photosynthesis [35], vision [36], and photostability of DNA [37, 38]. Acting as "doorways", CIs efficiently funnel the photoexcited WP to a lower-energy electronic state, facilitating nonradiative relaxation which occurs on a femtosecond timescale [31, 39].
In Figure (1.10), monodimensional and multidimensional representations of a CI are shown. The WP funneling occurs along a *reaction coordinate*, which may correspond to a photochemical reaction (e.g., as in photorhodopsin [36]), or a change in the molecular conformation [40, 41]. The two dimensions x_1 and x_2 define a *branching space*, where the WP propagates. These two coordinates are vibrational degrees of freedom that are generally a combination of changes in bond length and angles of the molecular structure of the species under investigation. The *reaction coordinate* is not necessarily one of these coordinates; rather, it is represented by the steepest descent path on the PES [32, 42].

CIs represent specific topologies within the PESs where two or more electronic states become isoenergetic, forming a multidimensional *seam* rather than just isolated points in space [34]. Depending on the local topography around the seam, CIs can be classified as either *peaked* or *sloped*, as shown in Figure (1.11). This topography significantly influences the ability of the CI itself to promote the nonadiabatic transition [43]. In a peaked CI, the WP is directed towards the intersection seam regardless of its initial approach direction, resulting in a more efficient conversion and triggering photochemistry. In contrast, a sloped CI exhibits less pronounced funneling characteristics,

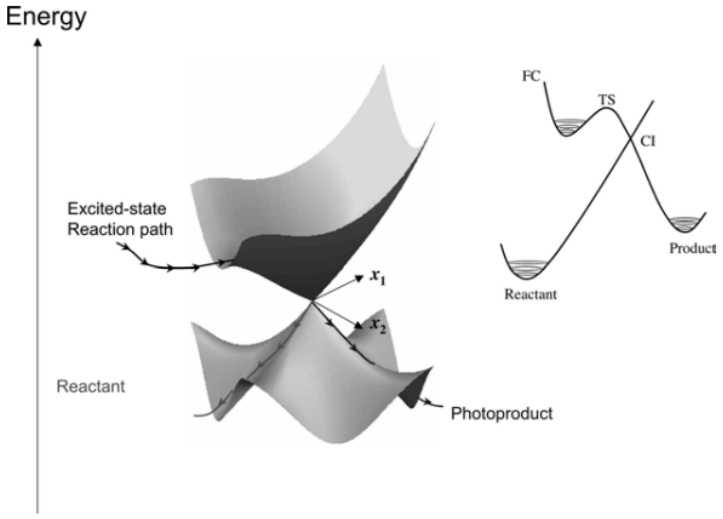

Figure 1.10: Cartoon illustration of a CI with a double cone structure, showing the excited state reaction pathway and two ground state reaction pathways (arrowed lines on the hypersurface). Coordinates x_1 and x_2 form the branching space. On the right, a monodimensional representation of the CI is reported to illustrate the mechanistic concept underlying these pathways. Abbreviations: FC, Franck-Condon excited state; TS, transition state. Reprinted from [42].

as the WP must "climb uphill" to reach the seam. This often leads to slower decay rates that do not involve photochemical processes [44, 45]. Controlling the topography around an intersection has been an intriguing area of research. This tuning was explored through variations in the surrounding environment [46, 47, 48] and by modifying the molecular structure, such as introducing different substituents [31, 49, 50].

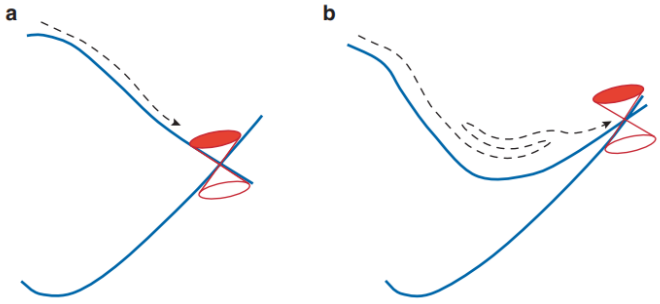

Figure 1.11: Schematic representation of peaked (a) and sloped (b) intersections. Reprinted from [51].

The simplest model employed in the description of CIs is the *two-state two-mode* (2S2M) model, which is illustrated in Figure (1.12). This model has been applied to relevant systems, such as photorhodopsin [52]. This framework introduces two electronic states and two vibrational modes to define the seam. The two electronic states can either be the ground state and the first excited

state or two energetically adjacent excited states. Regarding the vibrational degrees of freedom, the minimal configuration to model an intersection includes two vibrational modes: a *coupling mode* and a *tuning mode*. The coupling mode represents the interaction between the two PESs, while the tuning mode provides information on the energy shift between the two states. Typically, the tuning mode corresponds to a vibrational motion that reduces the symmetry of the system, thereby lifting the degeneracy between the electronic states and adjusting the energy gap [53, 54].
The main advantage of this model lies in its simplicity: it effectively captures the essential features of nonadiabatic transitions while remaining robust in its application. For this reason, this Thesis will adopt this model for data interpretation. However, it is important to note that the model's simplicity could be a disadvantage, as it might overlook additional states and modes that may be relevant to the dynamics [55].

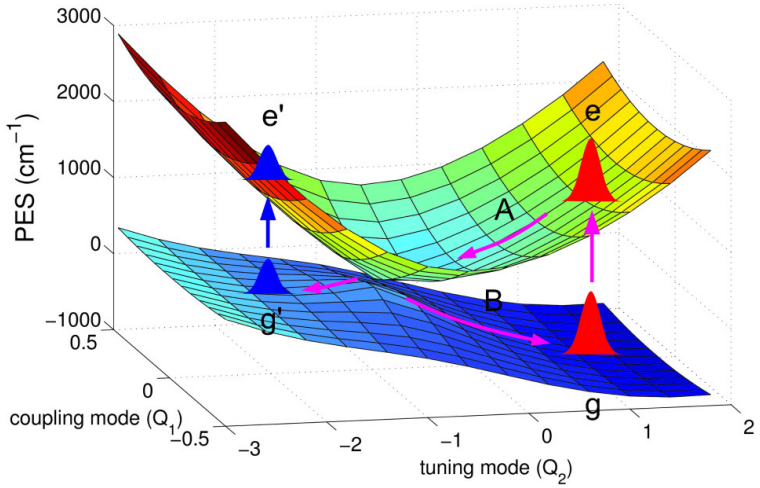

Figure 1.12: CI of two PESs illustrated as a function of the coupling and tuning mode. Transitions originating from the ground state are represented by vertical arrows, while the branching and evolution of the WP along the reaction coordinates are reported with pink curved arrows. Reprinted from [53].

An intriguing question is understanding the typical spectroscopic signatures of CIs and how these unique features can be captured experimentally. While it is relatively straightforward to calculate CIs using appropriate algorithms [56], their experimental detection remains challenging [45]. A primary characteristic of the dynamics at CIs in polyatomic molecules is the decay of the excited state population on timescales ranging from tens to a few hundred femtoseconds. Therefore, the presence of accelerated relaxation dynamics could serve as initial evidence of this phenomenon. [57]. However, it is desirable to identify signatures of a CI not only through the ultrafast nature of the nonradiative electronic decay but also through additional more robust spectroscopic information [53]. Another notable consequence of the presence of a CI in a system is the *Berry phase*, which is often considered the "smoking gun" for CIs in spectroscopic investigations [31]. The Berry phase is a specific type of geometric phase affecting the electronic wavefunction. This phase shift occurs during cyclical processes and is measurable. In an adiabatic system where the wavefunction is

dependent on nuclear coordinates, movement through parameter space results in the generation of a phase factor. To maintain the overall sign of the total wavefunction, the sign of the nuclear wavefunction changes in opposition to that of the electronic wavefunction [58]. The effect was generalized by Berry [59] and therefore is known as the Berry phase or geometric phase. As a consequence, the geometric phase can affect nuclear dynamics as the WP may interfere after being spread across the branching space along the possible pathways [60]. In light of this, the possible presence of time-dependent changes in the amplitude, frequency, and phase of the beatings relative to the time evolution of the vibrational WPs might represent a possible spectroscopic signature of the presence of a CI. In this context, 2DES, particularly sensitive to the time behavior of vibrational beatings, is predicted to be a powerful tool to capture clear evidence for CIs.

As a final consideration, it is important to note that various spectral signatures reported in the literature are highly dependent on the specific characteristics of each system. Consequently, the analysis of each system requires the development of specific tools. In Chapter 4, we will examine the spectral features of the studied squaraines using a combination of experimental data and different data analysis methodologies based on the predictions of the above-mentioned general models for CIs [53, 57, 61].

2 Squaraines

2.1 General Properties of Squaraine Dyes

Squaraine dyes are 1,3-disubstituted squaric acid derivatives. These dyes present a D-A-D π-conjugated system, where D represents the electron donor group while A denotes the acceptor moiety. Their general structure, as illustrated in Figure (2.1), highlights the zwitterionic nature of these dyes, promoted by the electron-deficiency of the central squaric ring [8, 62]. This structure facilitates an extensive charge delocalization, resulting in a quadrupolar charge distribution [63].

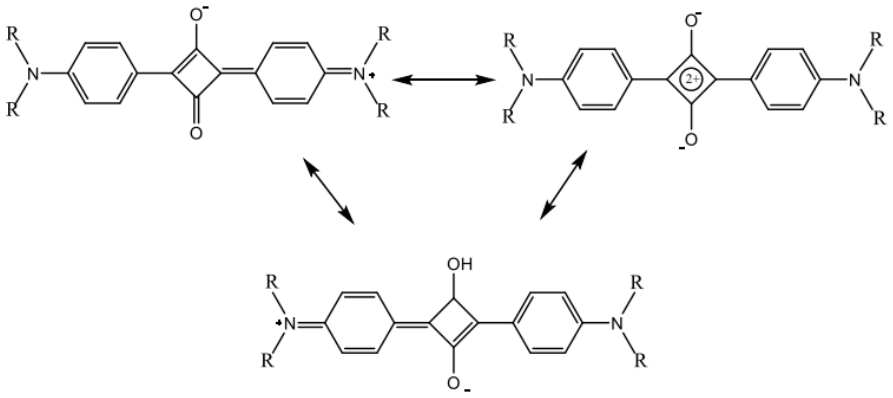

Figure 2.1: Resonance limit-structures for a generic squaraine dye.

Due to their rigid, planar, and zwitterionic nature, squaraines exhibit strong absorption, with molar extinction coefficients reaching up to 10^5 L mol^{-1}cm^{-1} [8], spanning from the visible (Vis) to the NIR region [9]. In combination with their flexible synthetic tunability and overall chemical stability, these characteristics make squaraines excellent candidates for the use as sensitizers in DSSCs [10].

In this Thesis, three symmetrical squaraine dyes were selected as sample compounds:

- 2,4-bis[4-(N,N-diisobutylamino)-2,6- dihydroxyphenyl] squaraine (**SQ**);
- 2,4-bis[4-(N,N-diphenylamino)-2,6-dihydroxyphenyl] squaraine (**DPSQ**);
- 2,4-bis[4-(N,N-dibenzylamino)-2,6-dihydroxyphenyl] squaraine (**DBSQ**).

These dyes are commercially available (Sigma-Aldrich®) and their structures are reported in Figure (2.2).
Unlike the general structure depicted in Figure (2.1), the selected compounds bear hydroxyl substitutions on the lateral phenyl groups. These groups enable intramolecular hydrogen bonding, which increases the rigidity of the conjugated system and thus enhances the dye's overall performance [8]. Additionally, they offer functional advantages by playing a critical role in binding to electrodes in DSSCs [64].

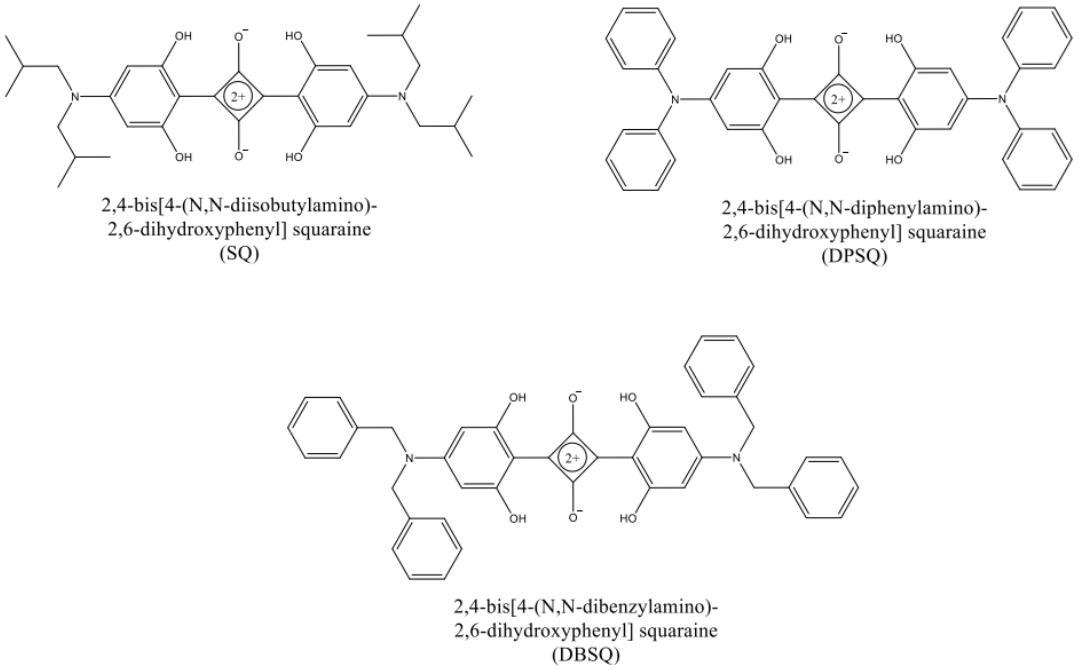

Figure 2.2: Molecular structure of the three squaraine dyes examined in this work.

Computational calculations conducted by Prof. Petrone and his collaborators at Università degli Studi di Napoli on these specific squaraine dyes have revealed that these molecules can adopt three distinct structural forms, in solution and at room temperature [65], as shown in Figure (2.3) for SQ. These conformations include the neutral planar (*p*-), neutral distorted (*d*-) and anionic (*a*-) form.

The planar structure is characterized by a symmetrical arrangement of the atoms, stabilized by a network of four intramolecular hydrogen bonds. In contrast, the distorted structure deviates from this highly symmetric conformation. This form is particularly noteworthy due to its potential impact on the electronic and vibrational properties of the dyes. Lastly, the anionic form, which emerges from an acid-base equilibrium, is non-planar and exhibits distinct electronic and spectroscopic properties compared to the neutral forms [65].

2.2 Sample Preparation

Preparing sample solutions with suitable properties is a critical step for 2DES measurements. First, we need to ensure that the samples have optimal absorbance to maximize nonlinear signals while minimizing excessive scattering during measurements. Therefore, it is necessary to choose a solvent that is able to solubilize the dye effectively. At the same time, the choice of solvent presents another challenge, as many solvents can interfere with signal detection. Thus, selecting an appropriate solvent requires a balance between achieving sufficient solubility and minimizing interference in the measurement process. This interference typically arises from the solvent's non-resonant signal, which combines with the system's signal to influence the overall response [66]. The strength

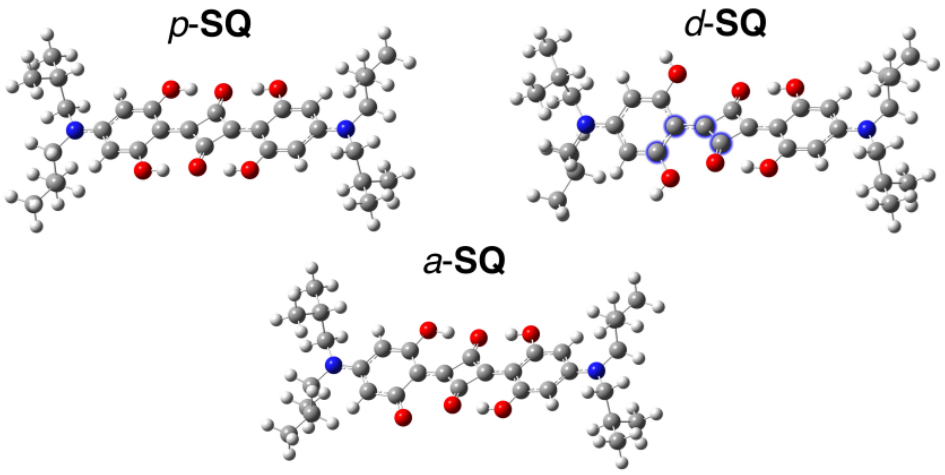

Figure 2.3: Computed conformations of SQ in acetonitrile; the (*p*-), (*d*-) with the angle involved in the distortion highlighted in blue and (*a*-) forms are depicted. Reprinted from [65].

of this signal depends on the solvent's nonlinear susceptibility [67]. Therefore, ensuring that the solvent response does not overlap with the sample's response is critical to capture the ultrafast dynamics of interest. For instance, although toluene effectively dissolves organic compounds such as squaraines, it is unsuitable for our purposes due to its strong third-order response, which can mask the relevant dynamics in our investigation.
Among the solvents tested, water and methanol exhibited minimal interference. Glycerol, ethanol, isopropanol, and acetonitrile were also deemed suitable for standard 2DES conditions. In contrast, solvents such as benzene, toluene, xylene, chloroform, and dichloromethane proved to be problematic in 2DES analysis [67]. All considered, acetonitrile emerged as the preferred solvent, offering an optimal balance in terms of solubility and minimal interference. To investigate the role of hydrogen bonding on the dynamics, methanol was selected as the best option among protic solvents with properties similar to those of acetonitrile.
As a result, five sample solutions were prepared: SQ, DPSQ, and DBSQ in acetonitrile, and SQ and DPSQ in methanol. DBSQ was only poorly soluble in methanol, and the resulting solution was also unstable over time; therefore, this sample was not considered for the ensuing characterizations.

2.3 Preliminary Spectroscopic Characterization

Acquiring preliminary data on the basic optical properties of the studied molecules is essential for the subsequent interpretation of the 2D spectra. To accomplish this, several linear spectroscopic techniques were utilized.
This Section presents the linear optical characterization of the dyes, using absorption (Agilent® Cary 100), fluorescence (HORIBA® FluoroMax-P), IR (FT-IR Bruker® Tensor 27) and resonant Raman spectroscopy. UV-Vis absorption and emission spectroscopies serve as a key preliminary step

to identify relevant electronic transitions, essential for interpreting the signals in 2DES, and to ensure that the samples have not deteriorated after the nonlinear measurements. Additionally, time-resolved fluorescence measured by time-correlated single-photon counting (TCSPC) was employed to assess the lifetime of the excited states, providing complementary information to the dynamics measured by 2DES. Finally, vibrational properties were investigated by IR and Raman spectroscopy; the obtained results offer valuable information on the molecular vibrations that might contribute to the beating behavior recorded in the 2DES response (see Section 1.5.1); further details on this specific topic are presented later in Section 3.2.2.

2.3.1 UV-Vis Absorption and Emission Spectra

Each of the analyzed samples exhibits a characteristic and rather narrow intramolecular charge transfer (ICT) absorption band between 600 and 700 nm [68, 69], as shown in Figure (2.4). This band corresponds to the $\pi - \pi^*$ transition between the HOMO and LUMO levels [70, 71].

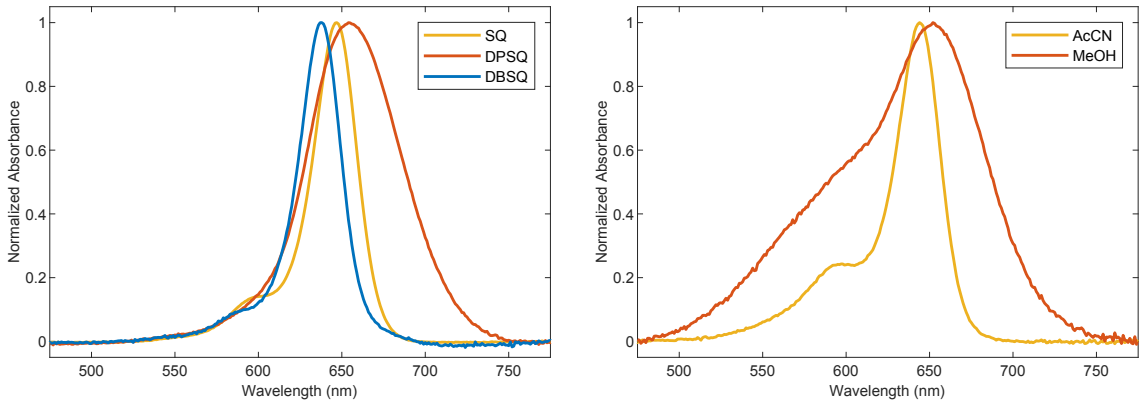

(a) Acetonitrile **(b)** Methanol

Figure 2.4: Normalized absorption spectra of SQ, DPSQ, and DBSQ in (a) acetonitrile and (b) methanol solutions.

The wavelengths corresponding to the maximum absorption (λ_{max}) of the samples are reported in Table (2.1).

Solvent	SQ, λ_{max} [nm]	DPSQ, λ_{max} [nm]	DBSQ, λ_{max} [nm]
Acetonitrile	647	657	638
Methanol	644	652	

Table 2.1: Summary of the maximum absorption wavelengths obtained from the UV-Vis spectra.

In acetonitrile, as visible in Figure (2.4a), SQ and DBSQ display a shoulder at 594 nm and 588 nm, respectively, which has been attributed to a vibronic progression [72]. Instead, DPSQ deviates from this trend and presents a significantly broader absorption bandwidth, when compared to the other samples. This suggests that, aside from the predominant contribution of the planar form,

which is expected to dominate the linear response because of its lower energy [65], other conformations might be significant in the solution at the equilibrium, leading to a broader spectrum that masks the vibronic shoulder.

The UV-Vis spectrum of DPSQ in methanol (Figure (2.4b)) shows a similar shoulder feature. To determine whether this shoulder is a result of the protic nature of the solvent, a solution in another protic solvent, ethanol, was prepared; its spectrum is shown in Figure (2.5).

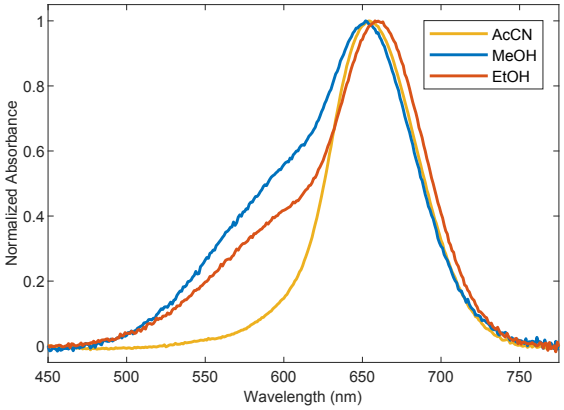

Figure 2.5: Normalized absorption spectra of DPSQ in acetonitrile, methanol, and ethanol.

In both methanol and ethanol, the shoulder is present and centered at $\sim$ 580 nm, which corresponds to the absorption of the anionic form, as confirmed by calculations and measurements on basified DPSQ solutions [65]. This might indicate that in protic solvents, the *a*-DPSQ form is stabilized due to hydrogen bond acceptors in the solvent, whereas such stabilization does not occur in aprotic solvents like acetonitrile. This also agrees with the pK_A estimations [65] and the linewidth of the band already commented. No further investigations were carried out on the ethanol sample due to its limited stability over time.

A crucial aspect of this photophysical characterization was ensuring that the solution contained only monomers. This was verified by recording absorption spectra of progressively diluted solutions. If the spectral shape remains unchanged with increasing dilution, it indicates that most likely no aggregate formation is present in the most concentrated solution. This verification is essential not only for this study but also for the intended application of squaraine dyes. Indeed, the presence of aggregates would be detrimental to DSSCs efficiency, as aggregation tends to quench intramolecular charge transfer, thereby reducing the electron injection efficiency from the sensitizer to the TiO_2 conduction band [9].

The experimental spectra shown in Figure (2.6) confirmed that no aggregates were formed, as no relevant changes were observed as a function of the concentration. This can be attributed to the presence of out-of-plane alkyl groups on the π-bridge, which were found to reduce the tendency for dye aggregation. Given the dyes' planar and quadrupolar π-conjugated structure, one would typically expect aggregation due to extensive $\pi - \pi$ intermolecular interactions. However, the sub-

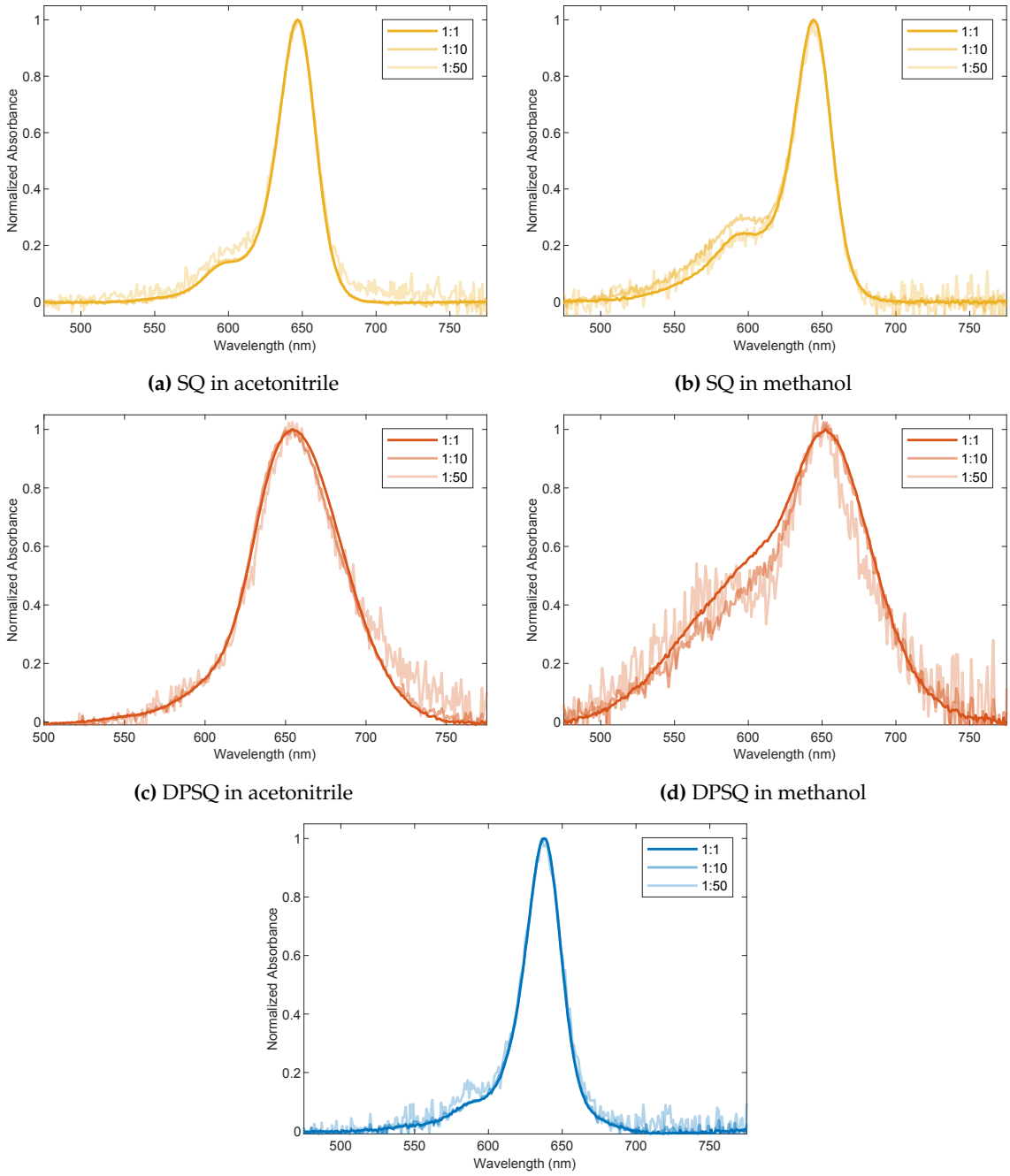

(a) SQ in acetonitrile

(b) SQ in methanol

(c) DPSQ in acetonitrile

(d) DPSQ in methanol

(e) DBSQ in acetonitrile.

Figure 2.6: Normalized absorption spectra of solutions prepared by successive dilutions (1:1, 1:10 and 1:50).

stituents act as isolating groups, effectively preventing dye-dye intermolecular interactions [8].

Fluorescence emission spectra were also recorded and are reported in Figure (2.7). The presence of a single band, corresponding to a single decay (as confirmed in the TCSPC analysis presented in the next Section), is an additional proof to support the presence of single monomeric species in solution. The characteristics of these emission bands are summarized in Table (2.2).

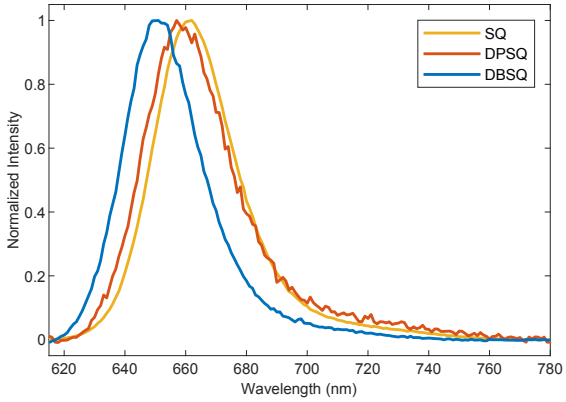

Figure 2.7: Normalized emission spectra for SQ, DPSQ, and DBSQ in acetonitrile. λ_{exc} = 610 nm for SQ; λ_{exc} = 615 nm for DPSQ and DBSQ. Emission spectra for the samples in methanol are omitted, as they are analogous to those shown here.

Solvent	SQ, λ_{em} [nm]	DPSQ, λ_{em} [nm]	DBSQ, λ_{em} [nm]
Acetonitrile	662	659	651
Methanol	658	652	

Table 2.2: Wavelengths corresponding to the maxima of the emission bands for the studied sample solutions.

2.3.2 Time-Correlated Single Photon Counting Technique

TCSPC is a time-resolved technique largely used to determine the fluorescence lifetime (τ_f) of dyes [73, 74]. This parameter is interesting because it relates to the DSSC efficiency, as seen in the definition of τ_f:

$$\tau_f = \frac{1}{k_{rad} + k_{non-rad}} \tag{2.1}$$

where k_{rad} and $k_{non-rad}$ are the decay rate constants associated with radiative and nonradiative processes, respectively.

In this work, the data were collected with a modified version of a HORIBA® FluoroMax, equipped with a pulsed nanoLED centered at 609 nm with a 1 MHz repetition rate and a 1.5 ns time resolution. After data collection, the lifetime constants τ_f were extracted by fitting the output decay with

a single-exponential function $f(\tau_f)$ [74]:

$$f(\tau_f) = be^{-\frac{t}{\tau_f}} \tag{2.2}$$

with b the pre-exponential factor. The most relevant results are shown in Figure (2.8) and summarized in Table (2.3). Note that only samples later examined via 2DES were reported.

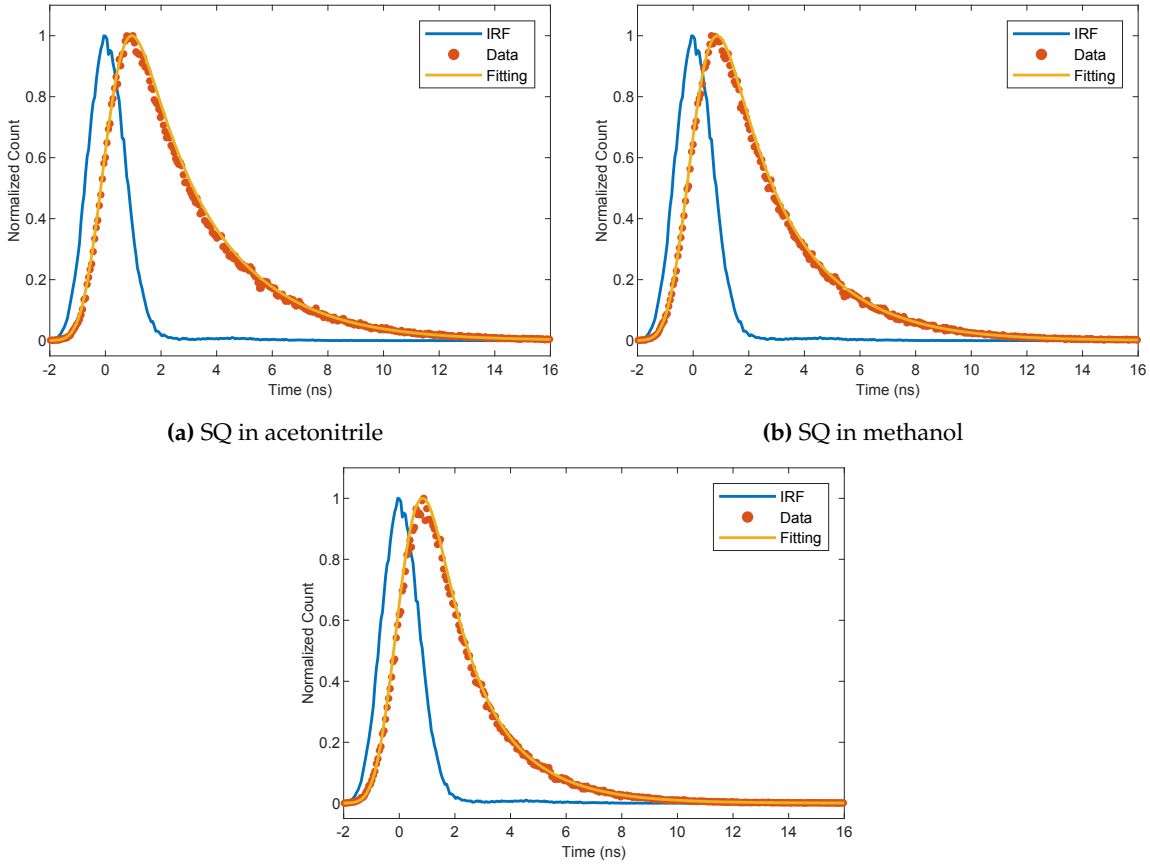

(a) SQ in acetonitrile

(b) SQ in methanol

(c) DBSQ in acetonitrile

Figure 2.8: TCSPC data of the three analyzed samples. The fitting curve is reported (yellow solid line), alongside the experimental data (orange dots), and the instrumental response function (IRF) (blue solid line).

These results indicate that the excited-state lifetime of SQ is minimally affected by solvent variations from aprotic to protic environment, as samples present similar fluorescence lifetimes within the experimental error. This suggests that the excited-state lifetime of SQ is not significantly influenced by changes in the hydrogen-bonding network surrounding the molecule. In contrast, variations in the peripheral N-substituents have a more pronounced effect on τ_f. It can be inferred that SQ's excited state is less susceptible to nonradiative processes in both solvents compared to DBSQ, likely attributable to its simpler molecular structure. A more detailed analysis of the nature of these nonradiative processes and the role of the N-substituents will be explored through the

Sample	τ_f [ns]	Error [ns]
SQ in AcCN	2.5	$\pm$0.2
SQ in MeOH	2.3	$\pm$0.2
DBSQ in AcCN	1.7	$\pm$0.2

Table 2.3: Measured fluorescence lifetime constants for the examined samples. Each constant is retrieved from a mono-exponential fitting and is reported with the corresponding error.

2DES analysis presented in Chapter 4.

2.3.3 Vibrational Spectra

The experimental IR and Raman spectra, respectively in Figures (2.9) and (2.11), were collected in the solid phase and are consistent with the computational results, where the vibrational analysis was performed in acetonitrile solutions [65]. A meaningful comparison can still be made by focusing on the main vibrational features.

Observing Figure (2.9), three key regions of interest can be identified:

i. 600-700 cm^{-1}. This region is dominated by collective out-of-plane aromatic C-H bending, addressed to DPSQ and DBSQ. For SQ, this range is characterized by modes associated with the lateral alkyl substituents [75].

ii. 1200-1400 cm^{-1}. In this spectral range, the most intense mode results in a ring breathing of phenolic rings, located at $\sim$1250 cm^{-1}.

iii. 1100-1750 cm^{-1}. This region encompasses collective and backbone modes for all studied squaraines. Such modes are asymmetric and symmetric stretching of C–C, C–O, and C–N bonds [65]. Notably, no C=O stretching at $\sim$1700 cm^{-1} is observed. This strongly indicates the extensive bond delocalization in the four-membered ring. Instead, strong absorption bands at $\sim$1600 cm^{-1} are observed and attributable to the C=C stretching in the squaric and the phenyl rings [75].

The computed IR spectra enabled the further exploration of the different conformations. The band around 1250 cm^{-1} was identified as the most sensitive to conformational changes, with a blue shift and reduced intensity observed for SQ, as shown in Figure (2.10). Applying the same hypothesis also to the other dyes, it becomes evident that the experimental spectrum of DPSQ, Figure (2.9b), displays a broader band around 1250 cm^{-1}, once again suggesting a significant contribution from non-planar conformations.

The same observations made for the IR spectra also apply to the Raman spectra shown in Figure (2.11), with further analysis provided for the most intense peaks:

i. $\sim$150 cm^{-1}. This peak corresponds to the breathing motion of the N-substituents in the donor moiety of each sample. Due to structural differences in these substituents, the exact frequency varies slightly among the samples (155 cm^{-1} for SQ, 140 cm^{-1} for DPSQ, and 148 cm^{-1} for DBSQ.)

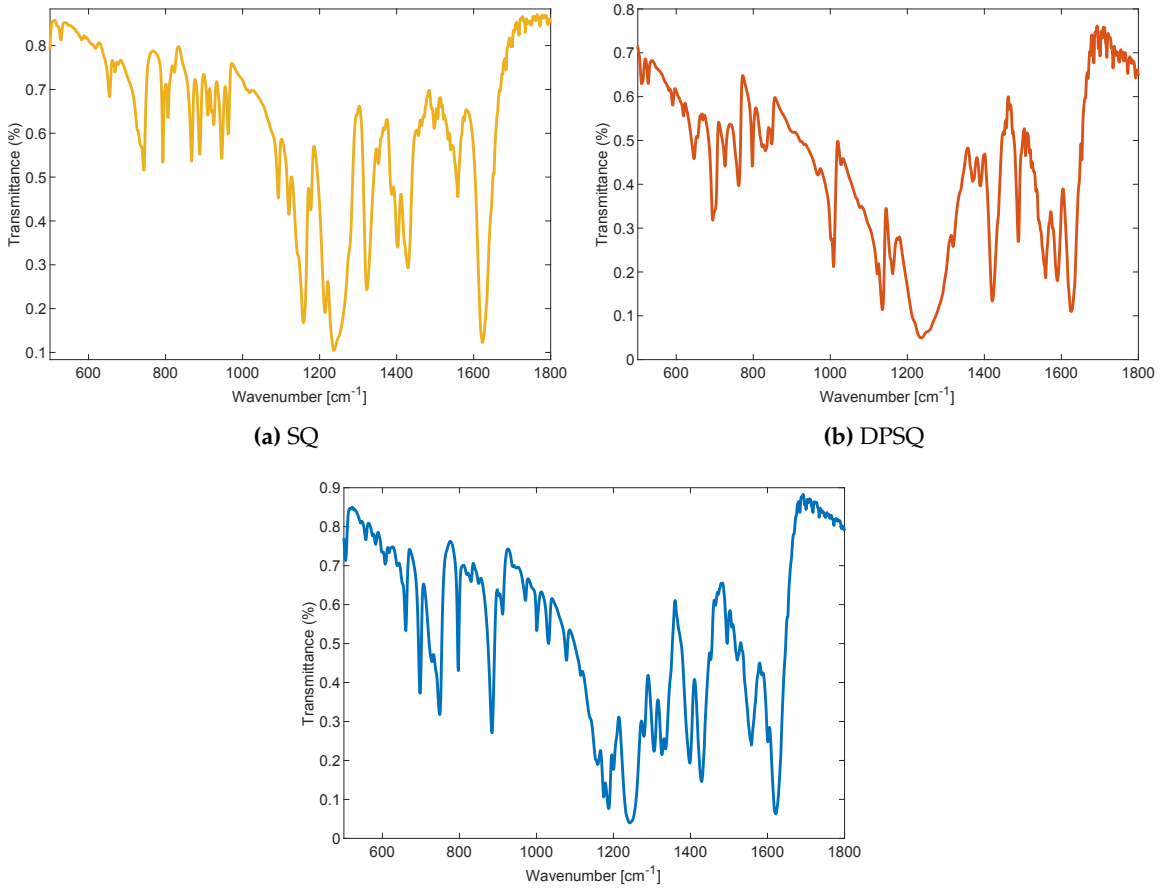

(a) SQ

(b) DPSQ

(c) DBSQ

Figure 2.9: IR spectra registered in solid state. The dyes, in powder form, were dispersed in KBr-pressed pellets.

ii. $\sim$450 cm^{-1}. Present in all three samples, this peak is especially prominent in DPSQ. For SQ and DBSQ, it is attributed to the combined breathing motion of the N-substituents and the central hydrogen bonds. In DPSQ, however, it corresponds to a unique vibration involving the out-of-plane motion of the N-phenyl substituents, which explains the observed deviation in intensity.

iii. $\sim$590 cm^{-1}. This peak represents the twisting motion of the phenolic rings relative to the squaric core.

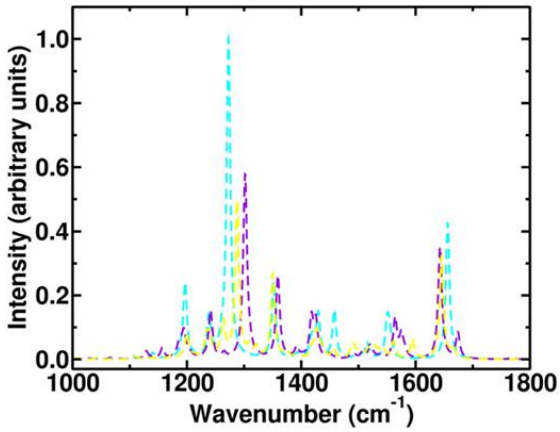

Figure 2.10: B3LYP/6-31+G(d,p)/C-PCM infrared spectra of different conformations and protonation states in acetonitrile solution. *p*-SQ cyan dashed line, *d*-SQ violet dashed line, and *a*-SQ yellow dashed line. Intensities were scaled with respect to the planar conformation, which is the most intense. Reprinted from [65].

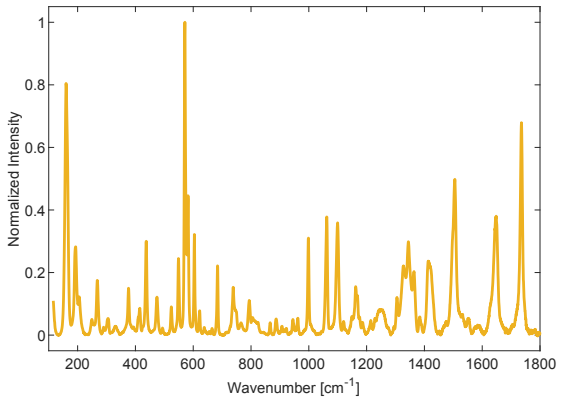

(a) SQ

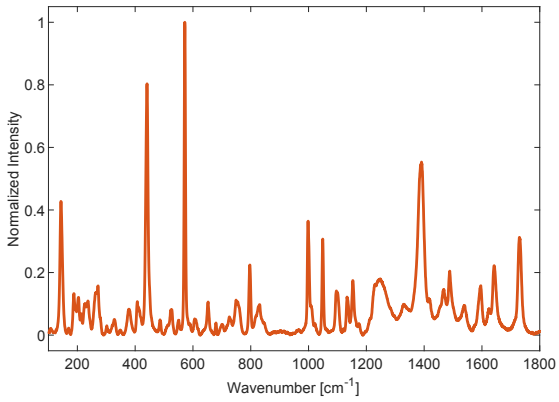

(b) DPSQ

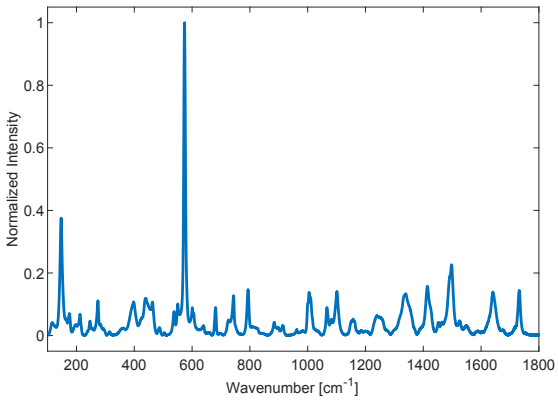

(c) DBSQ

Figure 2.11: Normalized Raman spectra; λ_{ecc}= 633 nm. The samples were analyzed in solid state at low temperature (T$\sim$ 160°C), to prevent damage.

3 Experimental Setup and Data Analysis

With the diffusion of ultrashort pulsed light sources in the late 1990s, transient spectroscopies gained access to the nano- and picosecond time domains. However, short light pulses have a broad energy spectrum due to the time-frequency uncertainty principle, which means that achieving good time resolution generally comes at the cost of losing frequency resolution. 2DES overcomes the Fourier limit, providing both high temporal resolution, to track dynamics occurring on the femtosecond timescale, and spectral resolution, to resolve excitation and emission energies over significant bandwidths with high spectral accuracy [76]. As mentioned in Chapter 1, 2DES offers several advantages and can provide more information than conventional 1D spectroscopies, but this comes at the expense of a more complex optical setup [77].

This Chapter offers a concise overview of the fully non-collinear 2DES setup used to investigate the ultrafast dynamics of the systems under study, along with the key steps in experimental and data analysis procedures.

3.1 Experimental Setup

This Section illustrates the components of the optical layout, schematized in Figure (3.1).

3.1.1 Laser Source and Light Conversion

The laser source is a Coherent® Libra laser based on an amplified Ti:Sapphire system. The source consists of three different subunits: a Ti:Sapphire oscillator (*Vitesse*), a regenerative optical amplifier (*Regen Cavity*) which is pumped by a Nd:YAG laser (*Evolution*).
The *Vitesse* oscillator initially produces a train of pulses, called *seed pulses*, at a wavelength of 800 nm. These pulses feature a duration of about 100 fs, a bandwidth of approximately 12 nm, and a repetition rate of 80 MHz, with each pulse possessing an energy of around 3.5 nJ.
The energy of the seed pulses is not high enough for many nonlinear experiments. Therefore, the pulses undergo an amplification stage within the *Regen Cavity*, where their energy is increased up to 100,000 times. The *Regen* contains a second Ti:Sapphire crystal where an inversion of population is generated by the *Evolution* laser, using pulses at 527 nm. To protect the Ti:Sapphire crystal from high peak power damage, the seed pulses are temporally stretched before amplification and compressed back to their original duration of 100 fs after amplification.
In the end, the output from the Libra system is a continuous train of pulses centered at 800 nm, with a repetition rate of 3 kHz and an energy of 0.8 mJ.

The laser pulses from the Libra source are then used to pump the Light Conversion® TOPAS White, an automated non-collinear optical parametric amplifier (NOPA), designed to convert the central wavelength of the pulses from 800 nm to a tunable value within the 500-1100 nm range. The amplification process in the NOPA system is facilitated by a supercontinuum light (white light) generated in a nonlinear crystal.
Upon entry, a beam splitter divides the incoming 800 nm beam into two components; 1% of the

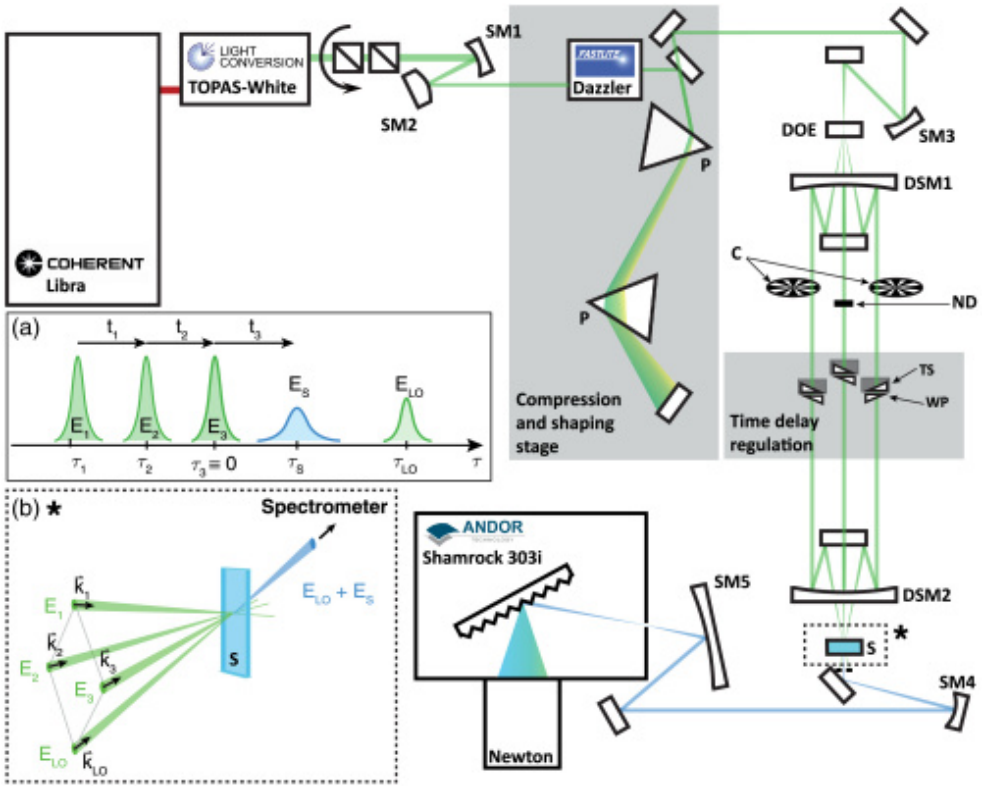

Figure 3.1: Schematic representation of the 2DES setup. Abbreviations: SM, spherical mirror; P, prism; DO, bi-dimensional diffractive optical element; DSM, donut spherical mirror; C, chopper; ND, neutral density filter; WP, wedge pair; TS, translational stage; S, sample.
Insert (a) describes the pulse sequence and the time intervals definition in a 2DES rephasing experiment. Insert (b) reports a schematic representation of BOXCARS geometry, where $\mathbf{E}_i$ are the three interacting fields, $\mathbf{k}_i$ are the wavevectors, and $\mathbf{E}_{LO}$ is the fourth pulse used for heterodyne detection. Reprinted from [77].

beam is focused onto a sapphire plate to produce the white light continuum. This white light is then collimated using spherical mirrors and directed into a pulse shaper that controls the chirp and bandwidth of the final amplified pulse. The remaining 99% of the pump beam is directed through a barium-boron-oxide (BBO) crystal ($Ba(BO_2)_2$) where a 400 nm pulse is generated via second harmonic generation (SHG). This converted beam is further split into a pre-amplification beam (5%) and a main amplification beam (95%). The white light and amplification beams subsequently interact in a second nonlinear BBO crystal; by adjusting the incident angles and delays of the three beams, it becomes possible to selectively amplify a specific range of the white light by rotating the crystal. The amplified beam is then collimated using a mirror telescope before exiting the TOPAS White.
At the end of this amplification stage, the output is a train of pulses with a tunable central wavelength ranging between 500 and 1100 nm, with a typical bandwidth of 80-100 nm, depending on the chosen wavelength. Each pulse has a time duration of approximately 20 fs and an energy ranging from 1 to 30 µJ, adjustable via neutral density filters.

3.1.2 Pulse Shaping and Compression

When broadband pulses pass through transmissive optical media, the frequency components propagate at different speeds due to the wavelength dependence of the refractive index. This phenomenon, known as *chirp*, results in phase distortions that broaden the pulse duration and compromise the time resolution necessary for 2DES experiments [78]. To ensure high-quality results, it is essential to achieve transform-limited (TL) pulses, which are the shortest possible pulses for a given bandwidth. A pulse is TL when its phase, $\phi(\omega)$, is a linear function of the frequency, ω. In our setup, a combination of a prism compressor and an acousto-optic programmable dispersive filter (AOPDF, Fastlite® Dazzler) is used to compress and shape the pulse to approach as much as possible the TL condition.

The prism compressor consists of two prisms with a well-characterized wavelength-dependent refractive index. The linear chirp is corrected by adjusting the distance between the prisms and the angle of incidence. Therefore, the prism compressor handles most of the chirp compensation; however, the AOPDF is necessary to perform fine adjustments. It utilizes a birefringent crystal coupled to a piezoelectric device that generates acoustic waves. These waves interact with the pulse, scattering different wavelengths at specific times to allow precise control of the phase and amplitude of each spectral component.

The alignment of the prism compressor and the AOPDF settings must be optimized to achieve the shortest possible pulse duration. This is done through an iterative procedure where all the parameters are modified while monitoring the pulse duration. The pulse duration is measured using a third-order technique called frequency-resolved optical gating (FROG). This step is crucial to ensure optimal performance, as the pulse duration should be as close as possible to the TL condition.

The FROG experiment uses the same setup as 2DES, ensuring that the pulse properties and operating conditions are consistent between the two experiments. The FROG measurement involves three ultrafast laser pulses interacting with a non-resonant third-order material, typically a solvent such as dimethyl sulfoxide (DMSO), within the same cuvette and sample position used for 2DES measurements. During the FROG experiment, the time delay between the first two pulses ($\mathbf{k}_1$ and $\mathbf{k}_2$) is set to zero, while the third pulse ($\mathbf{k}_3$) is delayed by a time T. At the sample position, the first two pulses interfere to form an optical grating that diffracts the third pulse, and the resulting diffracted signal is recorded along the signal emission direction. The delay T is typically scanned over a range of approximately 100 fs, from -50 to +50 fs. As this scan is performed, the time-frequency map is recorded, with the time delay T represented on the x-axis and the corresponding spectral frequencies on the y-axis, as shown in Figure (3.2).

For an ideal TL pulse, the signal is detected when the third pulse temporally overlaps with the first two, and it decays uniformly for all spectral components as the third pulse moves away from the overlap condition. After being integrated along the frequency axis, the signal is fitted with a Gaussian function. The full width at half maximum (FWHM) of this fit provides the pulse duration.

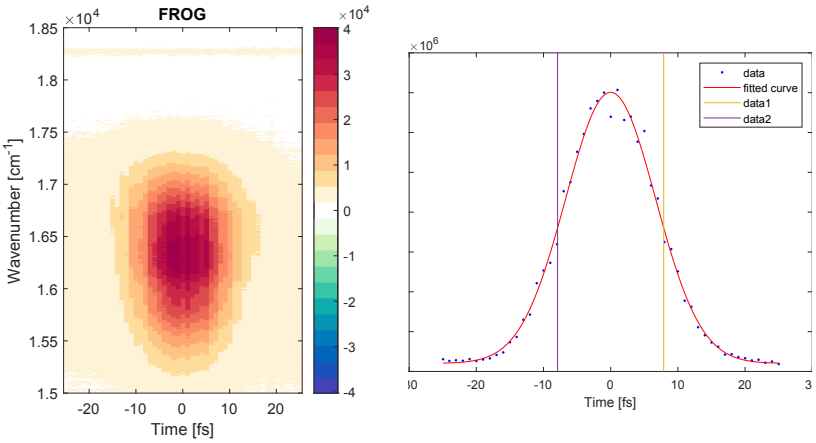

(a) **(b)**

Figure 3.2: Pulse characterization by FROG measurements. (a) Experimental pulse profile measured by the FROG experiment showing no relevant chirp effects. (b) Fitting of the FROG signal (integrated along the frequency axis) with a Gaussian function.

3.1.3 BOXCARS Geometry and Time Delay Regulation

Once the pulses are optimized, the beam is directed into the optical setup, where BOXCARS geometry ensures proper phase matching and pulse timing. To achieve this condition, the incoming pulse is split into four identical replicas by focusing it on a suitably designed two-dimensional diffractive optic element (DOE). After the DOE, the beams propagate parallel along the vertices of an ideal square, as shown in Figure (3.1b), and are focalized on the sample. Three of these beams serve as the exciting pulses, while the fourth, attenuated by a neutral density filter, is used as the local oscillator (LO), needed for detection purposes. Due to the phase-matching condition, the third-order signal is generated along the same direction as the LO.

Time delays between the exciting pulses are introduced using pairs of CaF_2 wedges; one wedge of each pair is mounted on a computer-controlled translation stage (Aerotech® Ant95). By adjusting the stage position, the overall thickness of the material crossed by the beam changes, controlling the time delay with a precision of about 0.07 fs. CaF_2 is preferred over the more common fused silica for its ability to minimize phase distortions in broadband pulses, leading to finer phase control. The fourth LO pulse is used as a time reference and thus remains fixed in its temporal position.

3.1.4 Heterodyne Detection

Due to the BOXCARS geometry, the third-order signal is emitted in the same direction as the LO, allowing for the two beams to interfere. The detection method is based on acquiring precisely

the interference between the emitted signal and the LO and is known as *heterodyne detection*. This methodology is known to be particularly advantageous in increasing the signal-to-noise ratio in case of very weak signals, like the third-order response measured in a 2DES experiment. The total intensity measured by the detector can be written as:

$$I_{TOT} \propto |E_{sig} + E_{LO}|^2 = |E_{sig}(t)|^2 + |E_{LO}(t)|^2 + 2\Re\left\{E^*_{sig}(t)E_{LO}(t)\right\} \tag{3.1}$$

After neglecting the signal intensity, which is much smaller than the other contributions, and subtracting the intensity of the LO (measured separately) the recorded intensity is linearly related to the electric field of the signal. This linear dependence significantly improves the signal-to-noise ratio.
Experimentally, the LO-signal interference passes through a spectrograph (Andor® Shamrock 303i), which disperses the light according to wavelength. The spectrograph has three gratings optimized for different spectral ranges, allowing for better resolution under varying conditions. Finally, the interference signal is recorded by a 5.5 Megapixel scientific complementary metal-oxide semiconductor (sCMOS) camera (Andor® Zyla).

3.1.5 Calibrations

Before performing any measurement, it is essential to ensure the phase-matching conservation and accurately calibrate the experimental setup. These procedures are essential in guaranteeing phase stability, which is crucial in obtaining meaningful 2DES maps.
The first step involves using a charge-coupled device (CCD) camera to confirm that the beam paths maintain the correct BOXCARS geometry without deviations during the wedges' motion. If any misalignment is detected, small adjustments can be made to the prism compressor and the wedges to optimize the alignment.
Then, the delay lines' calibration is performed: it links the position of each wedge (in millimeters) to the time delay (in femtoseconds) introduced for each pulse. The time delay calibration follows the linear relation:

$$\tau_i = c_i(x_i - z_i) \tag{3.2}$$

where τ_i is the time delay of the i^{th} pulse, c_i is the linear calibration coefficient in fs/mm, x_i is the position of the i^{th} wedge and z_i represents the zero-time position, at which all pulses have the same delay relative to the LO.

The typical calibration procedure involves placing a 25 μm pinhole at the sample position, where the four beams are focused. By recording the spectral interference between each pulse and the LO through the pinhole, the zero-time positions z_i can be determined. The calibration process proceeds through three main steps:

i. Evaluation of the zero time position z_i of the three linear stages that satisfy the condition $\tau_i(z_i) = 0$ fs.

ii. Evaluation of the linear coefficients c_i.

iii. Evaluation of the delay from the LO, τ_{LO}.

Additionally, calibration of the sCMOS camera is essential to associate specific wavelengths with each pixel. To achieve this, the AOPDF is used to create narrow 'holes' in the laser spectrum at specific wavelengths, which are then matched to the corresponding camera pixels. This procedure is repeated several times across the spectral range to ensure accurate wavelength-to-pixel association.

3.2 Data Processing and Analysis

The output of a 2DES measurement is a three-dimensional matrix that captures the interference between the signal and the LO, as a function of t_1, t_2, and emission frequency ω_3, as depicted in Figure (3.1a). The raw data contain both the signal and spurious scattering contributions, which must be removed before analysis. Therefore, a preliminary process to obtain the actual signal is crucial. Both pre-processing and data analysis are carried out using a home-written MATLAB® routine.

3.2.1 Preliminary Processing

The preliminary processing of the data is a complex procedure [77], whose exhaustive description goes beyond the aims of this Thesis. Therefore, only the main steps will be quickly summarized here. First, it is necessary to extract the pure signal from the interferogram, removing the scattering and the LO contributions. Then, a FT of the t_1 axis is performed to obtain the excitation frequency axis ω_1. At this point, the obtained signal is complex. To isolate the real and the imaginary components, the phase between the signal and the LO fields must be accurately estimated. This is done through a procedure called *phasing*, which is based on the projection-slice theorem [79]. We are particularly interested in retrieving the real part of the signal as it corresponds to absorptive phenomena occurring during the experiment [80]. This procedure is applied both to R and NR data. Then, after summation of the R and NR datasets, a third set of data is obtained, called the *total* (T) or *purely absorptive* signal. All the datasets at this point assume the form of 3D matrices where the signal (R, NR, or T) is reported as a function of ω_1, t_2 and ω_3.

3.2.2 Data Analysis

By examining the signal evolution along the population time, important insights into the system dynamics can be acquired, as described in Section 1.5.
Over the years, various approaches have been developed to analyze 2DES data [81, 82]. In our research group, a multi-exponential global fitting model has been developed for this purpose [83]. The fitting function is defined as:

$$f(\omega_1, t_2, \omega_3) = \sum_{n=1}^{N} a_n(\omega_1, \omega_3) e^{i\phi_n} e^{-\frac{t_2}{\tau_n}} e^{i\omega_n t_2} \tag{3.3}$$

This function fits the decay of signals at each (ω_1, ω_3) coordinate of the 2DES maps simultaneously. It efficiently extracts both the oscillating ($\omega_n \neq 0$) and non-oscillating ($\omega_n = 0$) components, each corresponding to a specific kinetic constant τ_n, without requiring prior subtraction of the oscillatory part.
The fitting returns two types of amplitude ($a_n(\omega_1, \omega_3)$) maps: 2D decay-associated spectra (2D-DAS) and 2D coherence-associated spectra (2D-CAS).

i. **2D decay-associated spectra**. These maps result from the fit of the non-oscillating components (where $\omega_n = 0$). The real part of the 2D-DAS reflects population dynamics and can be interpreted in comparison with the 2D maps: signals appearing with the same (opposite) sign at the same coordinates in 2D-DAS and the 2D maps, indicate an exponential decay (rise).

ii. **2D coherence-associated spectra**. These maps capture the oscillatory components of the signal. By fitting with complex exponentials, 2D-CAS provide information about the beating frequency ω_n, amplitude a_n, and phase ϕ_n of specific modes.

Alternatively, oscillations can be analyzed by removing the non-oscillating components, leaving behind oscillating residues. These residues can be integrated over both ω_1 and ω_3 and Fourier-transformed along t_2, resulting in a *Fourier spectrum of coherences* (FSC). This spectrum correlates the intensities of the beatings that oscillate along t_2 with their frequencies, allowing for easy identification of the main contributing frequencies. Comparing the FSC with the Raman spectrum can help differentiate vibrational coherences from other contributions, such as electronic coherences or solvent effects. If all the oscillations stem from vibrational coherences, the power spectrum should match the Raman spectrum [84].

An additional and robust approach to the oscillation analysis is to apply a *time-frequency transform* (TFT) to the oscillating residues. This analysis overcomes the limitations of conventional methods based on FTs, maintaining both frequency and time resolution. By combining bilinear and linear transforms, the TFT analysis produces a bi-dimensional plot where the signal is shown as a function of population time (x-axis) and the frequency of oscillating components (y-axis). TFTs provide both amplitude and phase information, offering a more comprehensive understanding of the oscillations' evolution and dephasing over time [85].

4 2DES Experimental Results

This Chapter presents the results obtained by applying 2DES to the following three samples: SQ in acetonitrile and methanol and DBSQ in acetonitrile. The other sample solutions initially prepared could not be investigated with 2DES because of insufficient solubility or stability.

Due to the extensive information that can be extracted from the 2DES response of the samples, for the sake of conciseness, the discussion will be first focused on analyzing the results achieved with SQ in acetonitrile, which serves as a benchmark sample due to its stronger signal.
Subsequently, we will explore how variations in different solvents and substituents may influence the overall dynamics by comparing the response of SQ in acetonitrile with that of SQ in methanol and DBSQ in acetonitrile, respectively.

The Sections below begin with an overview of the main spectral features observed in the 2DES maps, followed by a discussion of the population dynamics. Then, a detailed investigation of the oscillating dynamics is presented, using various data analysis methods.

Experimental Parameters. The experimental parameters for the 2DES measurements were the same for all samples. The experiments were run at room temperature employing an excitation laser bandwidth centered at 15870 cm^{-1} (630 nm), as shown in Figure (4.1), with a bandwidth of about 100 nm. The pulse duration was 12 fs, as determined by FROG measurement. t_2 was scanned from 0 to 1000 fs in steps of 7.5 fs, while t_1 was scanned from 0 to 90 fs in 2.3 fs increments. The exciting energy of the samples was set to approximately 7-8 nJ per pulse. R and NR experiments were performed for all the samples, each repeated three times to ensure reproducibility and improve the signal-to-noise ratio.

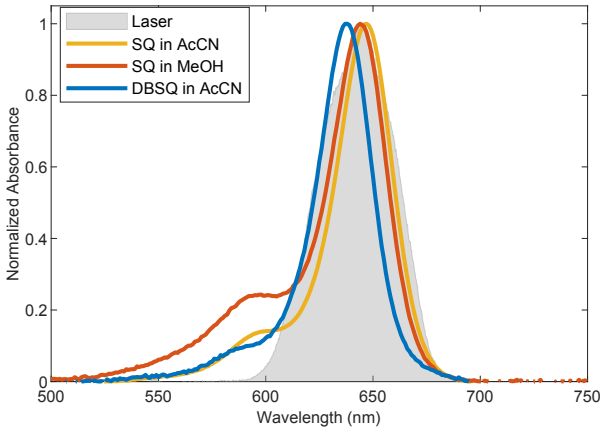

Figure 4.1: Spectral profile of the excitation pulse used in 2DES (shaded in gray). The colored solid lines represent the experimental absorption spectra of each sample, normalized and overlapped for comparison.

4.1 Evolution of 2DES Maps along the Population Time

The peaks observed in a 2DES map correspond to various processes occurring in the sample upon excitation, as described in Section 1.5. By analyzing the peak positions, it is possible to infer the energies of the levels involved in these processes, which helps to identify the transitions excited by the laser pulses.
Figure (4.2) shows the evolution of the 2DES signal for SQ in acetonitrile as a function of population time. Each 2D map represents a slice of the real part of the total 3D-matrix dataset, recorded at different values of the population time.

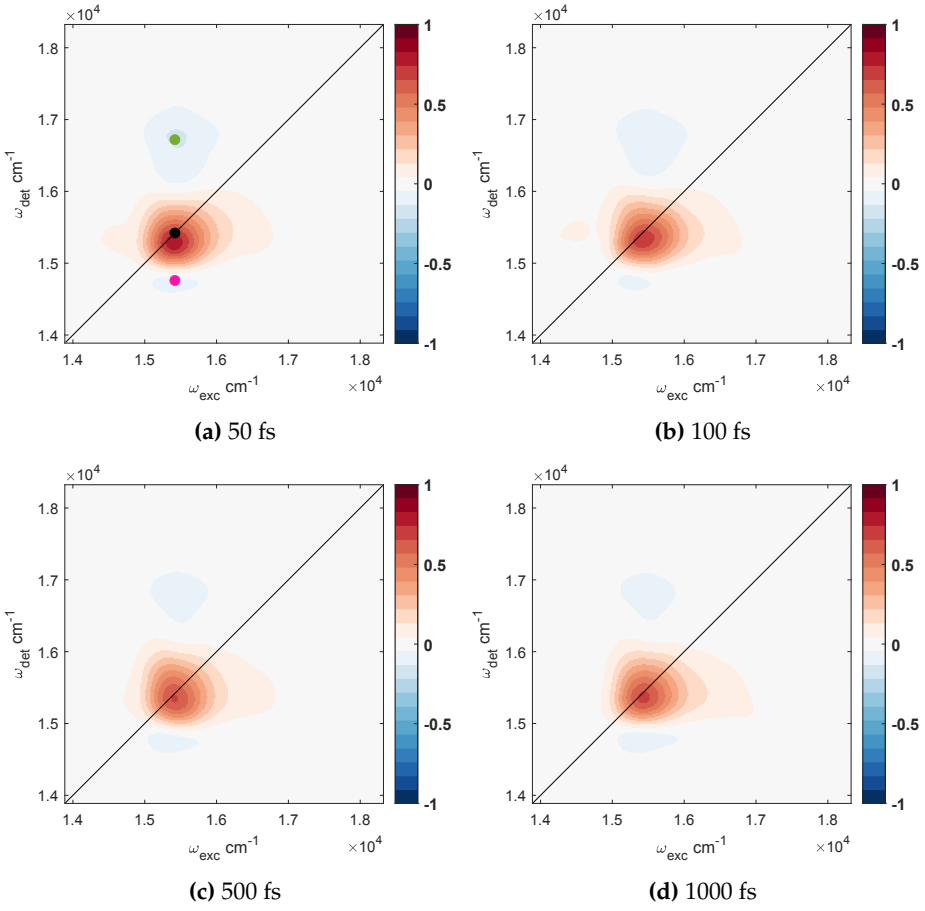

(a) 50 fs **(b)** 100 fs

(c) 500 fs **(d)** 1000 fs

Figure 4.2: Total real 2DES maps at selected values of t_2 for SQ in acetonitrile. In panel (a), the dots pinpoint specific relevant coordinates: green (15420, 16720) cm^{-1}, black (15420, 15420) cm^{-1} and magenta (15420, 14760) cm^{-1}.

The main feature of these maps is a positive diagonal peak at (15420,15420) cm^{-1} (black dot in Figure (4.2a)) attributed to the bleaching of the $S_1 \leftarrow S_0$ transition, as confirmed by both the UV-Vis spectrum and theoretical calculations [65]. Additionally, two off-diagonal negative features are visible below and above the diagonal, which can be attributed to ESA processes. Both features share the same excitation frequency as the positive peak, suggesting that the initially excited S_1 serves

as a starting point for both these ESA processes. The lower peak (magenta dot in Figure (4.2a)), hereafter referred to as ESA1, is centered at (15420, 14760) cm^{-1}, while the upper one (green dot in Figure (4.2a)), ESA2, peaks at (15420, 16720) cm^{-1}. Further insights into the dynamic processes giving rise to these ESA signals can be achieved by analyzing the time evolution of their amplitude. Looking at the evolution of the maps as a function of t_2 (Figure (4.2)), ESA2 shows its maximum amplitude immediately after photoexcitation. Then it undergoes a gradual decrease in intensity. This observation indicates that ESA2 originates directly from the first excited state initially populated by the exciting sequence, i.e. S_1, and suggests that ESA2 can be attributed to an $S_n \leftarrow S_1$ transition. Indeed, the decay of ESA2 intensity follows the same dynamics as the positive diagonal peak one, indicating a correlated depletion of the S_1 population. ESA1 displays completely different dynamics, with a signal amplitude that increases after approximately ∼100-150 fs. This behavior implies a two-step process: first, the population initially prepared on S_1 must relax to a lower energy state (denoted here generally as S^*), after which the ESA will occur starting precisely from S^*. Figure (4.3) proposes a first graphical interpretation of these processes.

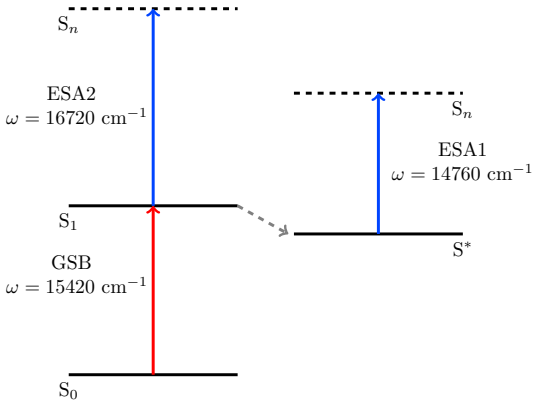

Figure 4.3: Level diagram summarizing the processes involved in the SQ photophysics captured by 2DES. Transition frequencies are reported in wavenumbers (cm^{-1}). Blue (red) arrows pinpoints ESA (GSB) processes. The gray dashed arrow indicates nonradiative population transfer.

To support the previous hypothesis, a more quantitative analysis based on the global fitting of the maps has been performed, as presented in the next Section.

4.2 Non-oscillating Signal Analysis

The global fitting analysis identified three non-oscillating decay components: two in the ultrafast regime, of 10 and 166 fs, and one with a significantly larger time constant ($\gg$ 1 ps). Each of these time parameters is associated with a 2D-DAS, which reports the amplitude distribution of the non-oscillating signal as a function of excitation and detection frequency, as shown in Figure (4.4). As already described in Section 3.2.2, the evolution of the system can be deduced by comparing the 2D map and the 2D-DAS at specific coordinates.

The first ultrafast component (Figure (4.4a)) exhibits a complex signal distribution. Such a short

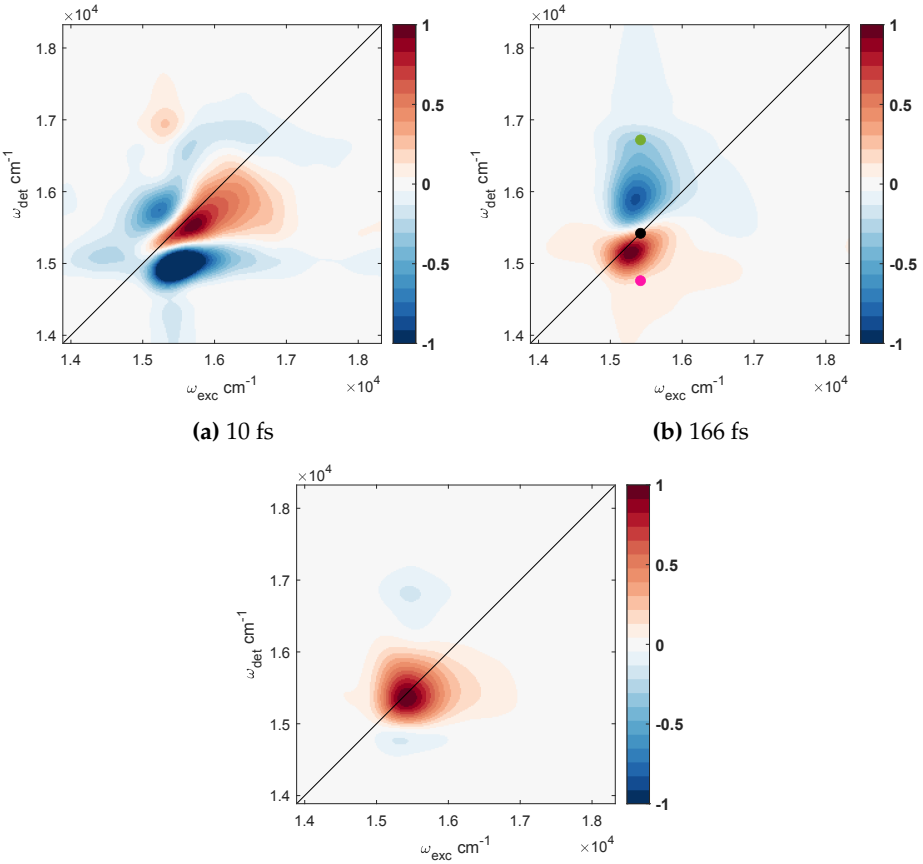

(a) 10 fs **(b)** 166 fs

(c) $\gg 1$ ps

Figure 4.4: 2D-DAS corresponding to the three times constants obtained from the global fitting analysis of the dataset obtained for SQ in acetonitrile. The intensities are normalized for ease of visualization. In panel (b) the dots pinpoint the same relevant coordinates as in Figure (4.2a): green (15420, 16720) cm^{-1}, black (15420, 15420) cm^{-1} and magenta (15420, 14760) cm^{-1}.

time constant may correspond to several processes, including phenomena not directly related to the photophysics of the studied dye, such as laser pulse overlap, scattering, and coherent artifacts. Nonetheless, the distinctive shape of the signals, with a positive diagonally elongated peak surrounded by two negative peaks symmetrically below and above diagonal, present the typical features commonly attributed to spectral diffusion, which is a time-dependent broadening of the electronic transition due to the interaction with the environment (including the coupling with vibrational degrees of freedom and with the solvent molecules) [22, 86]. While spectral diffusion for organic molecules in solution is generally associated with slightly longer time constants [87], it has been observed that when anharmonic coupling between high-frequency and low-frequency intramolecular vibrational modes is present, the spectral diffusion rate tends to increase [88]. As discussed later in the oscillating analysis presented in Section 4.3, this could be the case. Additionally, another notable feature in Figure (4.4a) is the prominent negative peak below the diagonal. Literature reported that such a signature can be typically attributed to the relaxation from higher

to lower energy states [89]. This could be interpreted as the relaxation from the vertically excited FC state to the relaxed configuration within the same potential energy surface, similar to what has been already found for other red-absorbing dyes [90].

The second ultrafast 2D-DAS (Figure (4.4b)) reveals two distinct features centered at around ω_{exc}=15420 cm^{-1}: an intense off-diagonal negative (blue) peak, that extends over higher detection frequencies and a diagonal positive (red) peak that spreads towards lower ω_{det}. To understand the underlying dynamics, we compare the signs of the signal at the coordinates marked by dots in Figures (4.2a) and (4.4b). At the coordinates pinpointed by the black and green dots, the signal in the 2D maps and the one in the 2D-DAS have consistently the same sign, meaning that at these coordinates the signal is decaying with the same time constant of 166 fs. Instead, at the coordinates of the magenta dot, the signal sign indicates that the amplitude is rising, again with a time constant of 166 fs. Given this information, it can be concluded that with a time constant of 166 femtoseconds, some of the population initially prepared in the S_1 state is transferred to another state, referred to as S*. This transfer leads to a second ESA (ESA1), the intensity of which follows the dynamics of the population transitioning from S_1 to S*. At this point, the focus turns to understanding the nature of the still unspecified S* state. One possible hypothesis is that the state in question is a dark state (because it is not detected in the absorption spectrum), lying at a lower energy than S_1. However, for quadrupolar systems like this one [91], dark states below S_1 are typically not expected. Furthermore, the $S_1 \leftarrow S_0$ transition has been confirmed to involve the HOMO and LUMO [65, 68, 69]. A second possibility is that S* represents a relaxed configuration associated with the S_1 surface, which can be reached through a relaxation process starting from the initially populated FC state. However, when considering the overall dynamics, it is important to note that this process has already been linked to the shortest time constant due to the peculiar amplitude distribution observed in the corresponding 2D-DAS. The third most likely possibility is that S* is the product of the crossing of a CI, associated, for example, with a different distorted geometry of the molecular structure. The sequence of these two processes—relaxation from the FC state and crossing of a CI—is plausible since CIs typically lie at lower energy compared to the vertically excited FC state [56]. Moreover, the presence of planar and distorted molecular geometries have been already verified also from the theoretical point of view, as described before [65].
The dynamic behavior shown in Figure (4.5) closely matches the trends predicted for a CI described by the 2S2M model [53], both in terms of the shape of the signals and timescale of the involved processes [57].

To better read the dynamics behind these two processes described, Figure (4.6) graphically reports the two discussed phenomena.

The last 2D-DAS reports a long time constant, due to dynamics that extend well beyond the experimental range. Its main feature is a positive diagonal peak, which corresponds to the final relaxation of the system to the ground state. This relaxation occurs with a time constant that exceeds the experimental time window [14, 92]. This observation agrees with the preliminary characterization reported in Sections 2.3.1 and 2.3.2, where a significant fluorescence signal was reported, and fluorescence lifetimes in the ns regime were recorded.

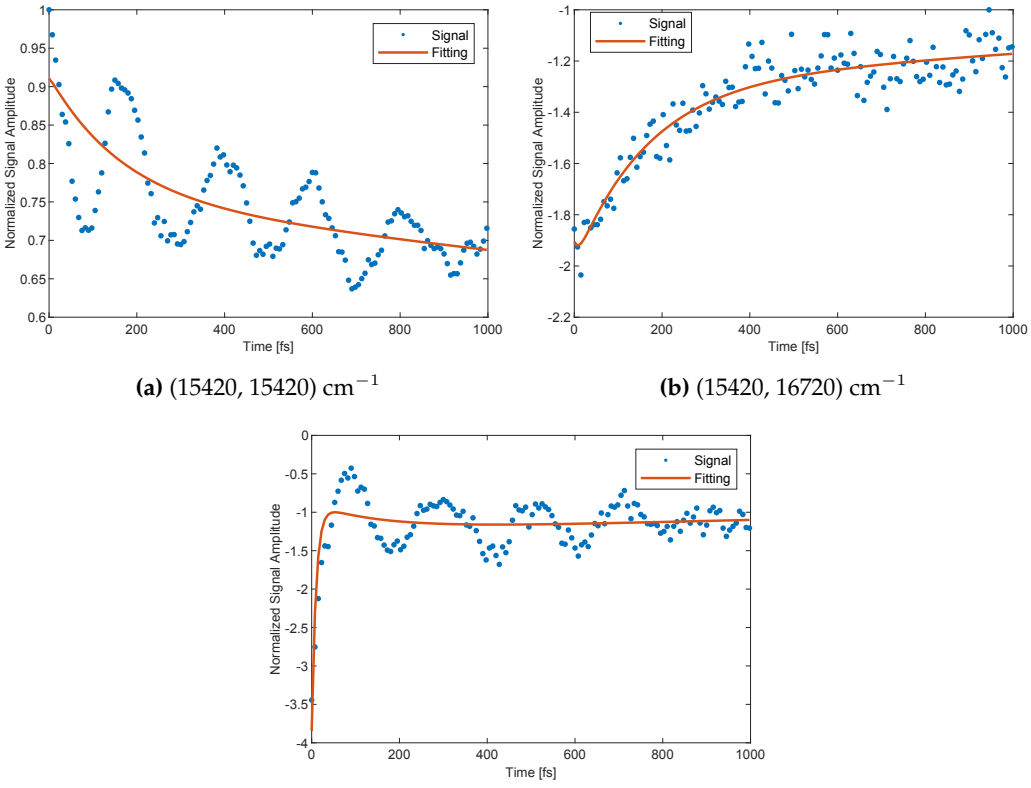

(a) (15420, 15420) cm^{-1}

(b) (15420, 16720) cm^{-1}

(c) (15420, 14760) cm^{-1}

Figure 4.5: Experimental decays (blue dots) and fitting traces (orange solid lines) at selected coordinates, as pinpointed by the colored markers in Figure (4.4b). At this stage, the oscillations were not included in the fitting.

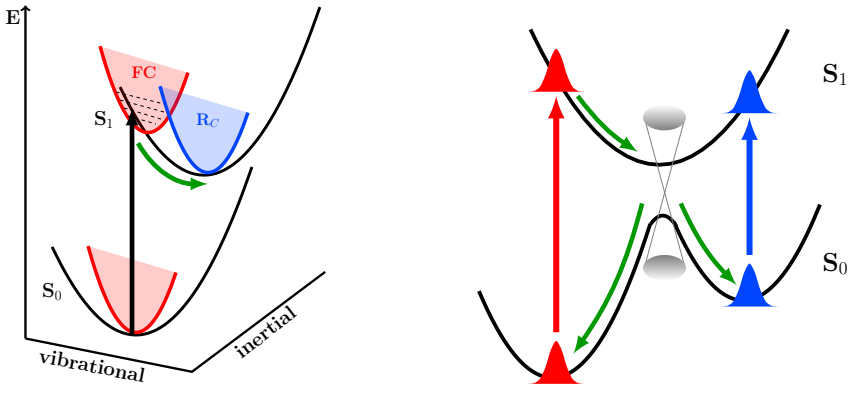

(a) **(b)**

Figure 4.6: Graphical representations of the possible ESA1 origins. (a) Relaxation from the vertically excited FC state to the relaxed configuration at the local minimum of the PES (R_C). (b) Crossing of a CI (drawn in gray) within a 2S2M model. In both diagrams, the green arrows show the WP pathway.

Typically, the presence of a CI leads to highly efficient nonradiative deactivation of the excited state [38, 57]. In this case, a comparison of the intensity of the diagonal peak in the second and third 2D-DAS suggests that the CI contributes to only about 25% of the overall deactivation and justifies the fluorescence behavior previously mentioned.

In Section 1.6, we highlighted how the role of beatings is crucial in defining and characterizing CI dynamics. As discussed in the next Sections, the analysis of these beatings will be essential for both confirming the presence of a CI and gaining deeper insights into its properties.

4.3 Oscillating Signal Analysis

An initial examination of the signal evolution as a function of t_2 (Figure 4.5) reveals strong oscillations superimposed on the signal decay. These oscillations arise from a combination of various beating components, stemming from different physical pathways that guide the system into different states during t_2. To identify the frequencies of the oscillations and analyze their time evolution, several approaches were employed, as previously described in Section 3.2.2.

4.3.1 Fourier Spectrum of Coherences

As described in Section 3.2.2, the FSC highlights the beating modes that are most strongly coupled with the resonantly excited transition. The intensity of each mode in the FSC correlates with the strength of this coupling [84]. When interpreting this type of spectrum, it is essential to consider a frequency error of $\pm$ 60 cm^{-1}, due to experimental resolution. Additionally, modes with frequencies below 100 cm^{-1} are excluded, as artifacts from the fitting procedure may heavily affect the actual frequencies [83]. The FSC obtained by Fourier transforming the oscillating residues of R and NR signals are reported in Figure (4.7).

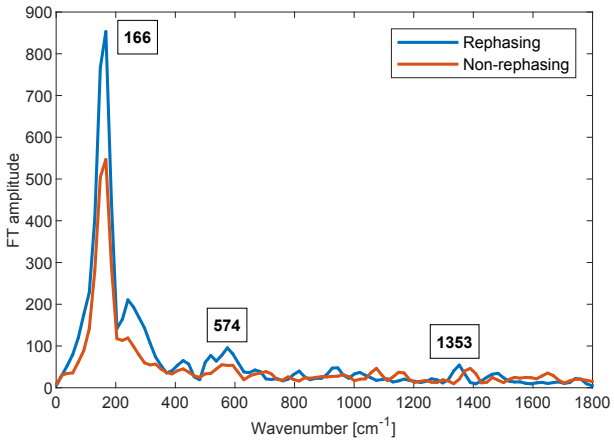

Figure 4.7: FSC of SQ in acetonitrile for the rephasing (blue) and non-rephasing (orange) response. The main signals are labeled.

Three main coupled modes were identified. Their attribution to specific vibrational modes is based on the calculations performed by Prof. Petrone and coworkers and on the comparison with the Raman spectrum [65] as:

- 166 cm^{-1}: is the most intense signal in the FSC, attributed, within the experimental error, to the 155 cm^{-1} mode that represents the breathing motion of the N-diisopropyl substituents.
- 574 cm^{-1}: reasonably corresponding to the 580 cm^{-1} mode, which involves the twisting motion of the phenolic rings with respect to the squaric core.
- 1353 cm^{-1}: this frequency corresponds to the 1361 cm^{-1} mode, describing the O-H motions around the phenolic fragments.

These three modes, depicted in Figure (4.8), altogether are responsible for inducing significant distortions in the molecule. These distortions are primarily localized around the central part of SQ, specifically at the junction of the squaric core and phenyl rings. It can be inferred that these deviations from the planar structure have an impact on the electronic transition.

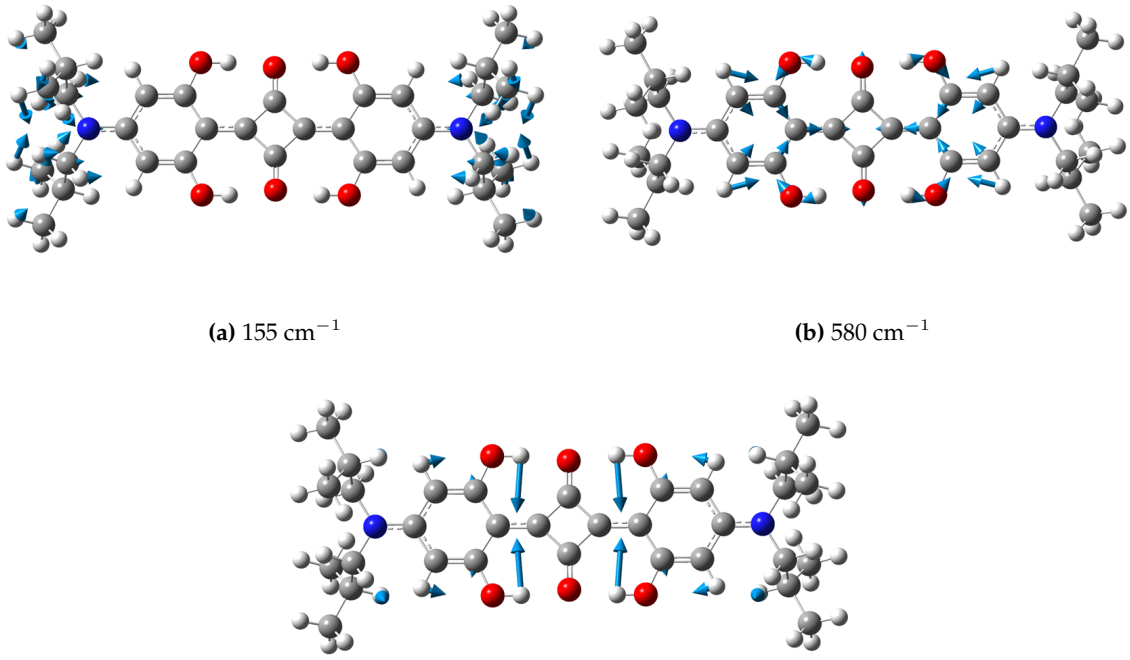

(a) 155 cm^{-1}

(b) 580 cm^{-1}

(c) 1361 cm^{-1}

Figure 4.8: B3LYP/6-31+G(d,p)/C-PCM (acetonitrile) infrared vibrational mode for *p*-SQ found at 155, 580 and 1361 cm^{-1}. Data provided by Prof. Petrone and coworkers.

4.3.2 Coherences Associated Spectra

An alternative method to analyze the beatings contributing to the 2DES response involves directly including the oscillating components in the global fitting procedure. The output of the global fitting analysis including both the non-oscillating and oscillating contributions is summarised in Table (4.1); moreover, we report the fitting traces in Figure (4.9) for the three selected coordinates already discussed above (pinpointed with dots in Figures (4.2a) and (4.4b)).

Component index n	1	2	3	4	5	6
Frequency ω_n [cm^{-1}]	0	0	0	160	589	1357
Time constant τ_n [fs]	10	166	>1000	600	>1000	>1000

Table 4.1: Output parameters of the global fitting including the oscillating components for SQ in acetonitrile (see Equation (3.3)).

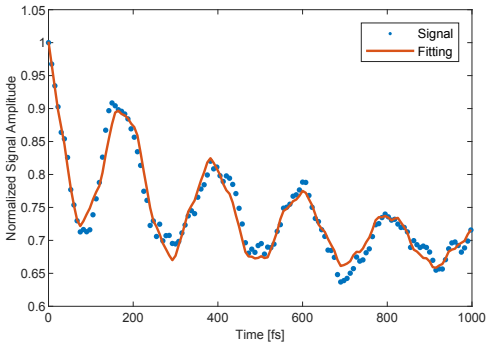

(a) (15420, 15420) cm^{-1}

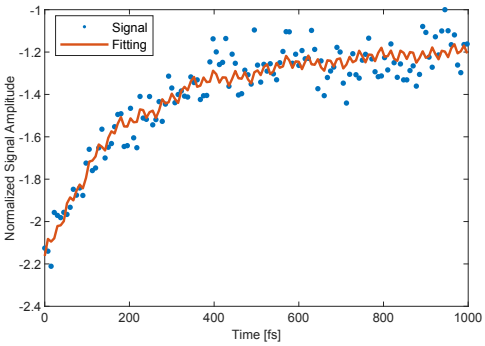

(b) (15420, 16720) cm^{-1}

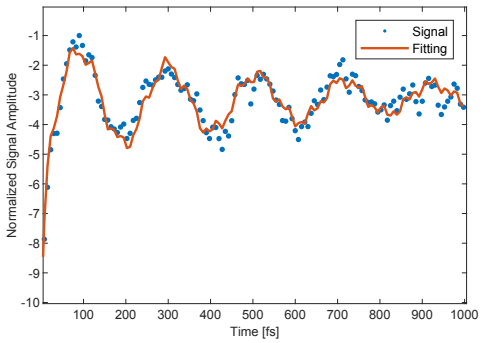

(c) (15420, 14760) cm^{-1}

Figure 4.9: Experimental signal (blue dots) and fitting traces (red solid lines) at selected coordinates. Both non-oscillating and oscillating components are included.

The reliability of the global fitting approach is demonstrated by the good agreement between the frequencies of the oscillating components found by the fitting and those obtained through the Fourier transform-based methodology discussed in the previous Section, as all of the three modes considered find correspondence in the fitting output. Indeed, the fitting reveals three main beating

components with frequencies of 160, 589, and 1357 cm^{-1}, which correspond well to the values of 166, 574, and 1353 cm^{-1} of the FSC. An additional piece of information that could be extracted from this kind of analysis is, along with the frequency of the beatings, also their dephasing times. In this case, the long dephasing time of the oscillations (all in the ps time scale) confirms the vibrational nature of these coherent beatings.

The amplitude associated with each frequency mode is plotted in the form of a 2D-CAS map, which is conceptually analogous to the 2D-DAS but refers to the oscillating components. The signal distribution in each 2D-CAS shows the coordinates where these oscillations contribute the most. The 2D-CAS for SQ in acetonitrile are shown in Figure (4.10); for each, both R and NR datasets are included and the frequency components are categorized as positive or negative. Positive and negative frequencies correspond to beatings that affect the regions below and above the diagonal in 2DES spectra, respectively [93].

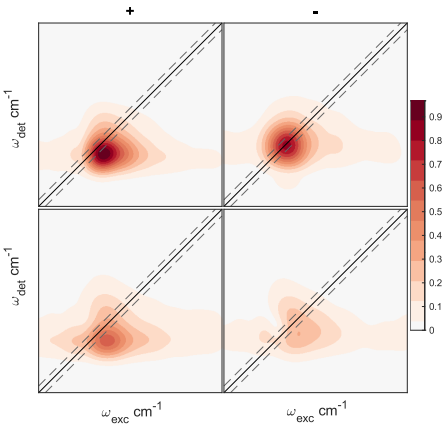

(a) 160 cm^{-1}

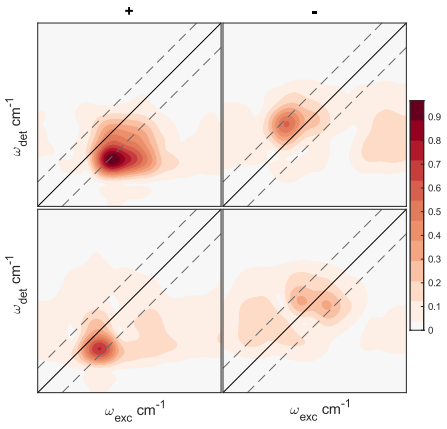

(b) 589 cm^{-1}

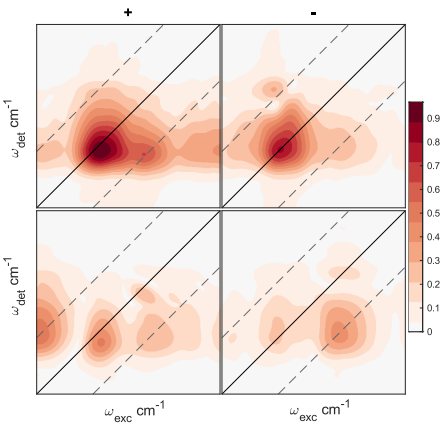

(c) 1357 cm^{-1}

Figure 4.10: 2D-CAS maps relative to the three main vibrational modes coupled with the electronic transition for SQ in acetonitrile.

Typically, the signal distribution in the 2D-CAS associated with each vibrational mode can be explained by invoking the DHO model, as outlined in Chapter 1. According to this model, a vibrational mode coupled with the resonant electronic transition should exhibit a chair-like distribution of signals in the corresponding 2D-CAS. Already at a first qualitative inspection of the 2D-CAS in Figure (4.10), it is clear that this model is not able to fully justify the amplitude distribution recorded experimentally. One plausible explanation for this peculiar distribution can be achieved by introducing a *multi-vibrational mode coupled DHO model* [27, 94]. This model applies when two or more vibrational modes are anharmonically coupled and account for signal contributions at novel and distinct coordinates. In addition to the anticipated chair-like pattern for the specific vibrational mode, signals directly related to the coupling between modes emerge. These contributions manifest at coordinates corresponding to the sum and difference of the frequencies of the coupled modes [27]. This is illustrated in Figure (4.11), where the basic DHO patterns are highlighted in blue while the additional contributions are marked in red. To fully explain these intricate patterns, it is necessary to define the associated Feynman diagrams, a complex procedure that was already undertaken in a precedent work within our group. For further details refer to [92], which discusses the case of this specific sample.

The detection of clear signatures of multi-mode coupling in organic chromophores is noteworthy, as it is relatively uncommonly displayed in the literature [95, 96, 97, 98]. Furthermore, this phenomenon points to a highly anharmonic behavior in the system under study, which was already noted through the presence of particularly fast spectral diffusion dynamics (see 2D-DAS analysis in Section 4.2).

4.3.3 Time-Frequency Transforms

To gain insight into the time evolution of vibrational coherences, a TFT analysis was also conducted. In relation to previous analyses, this approach can offer valuable insights into potential shifts in the frequency of the beatings at a specific coordinate, depending on t_2. This information is particularly critical, as these behaviors are indicators of the presence of a CI, as described in Section 1.6. Figure (4.12) shows the results obtained by applying the TFT analysis to the decay trace extracted at a specific coordinate where, in agreement with the 2D-CAS analysis, we expected to mainly capture the two lowest frequency modes at 160 and 589 cm^{-1}. Indeed, the plot reveals two main features, centered at the expected frequencies of about 160 cm^{-1} and 589 cm^{-1}, that present distinct temporal behaviors. The 160 cm^{-1} signal exhibits a notable evolution within the first 200-300 fs, characterized by a red shift of the frequency alongside an increase in intensity, which then decays after 300 fs. In contrast, the 589 cm^{-1} mode, which is less intense because of the particular choice of the coordinate, remains constant, both in amplitude and frequency.

The time evolution of the lowest-frequency mode is distinctive and may indicate the presence of a CI. As discussed in Section 1.6, it is expected that when a CI is present, the corresponding coupling mode may experience a frequency shift during the crossing, followed by a notable decrease in beating intensity once the CI is passed. In this case, the mode at 160 cm^{-1} appears to behave pre-

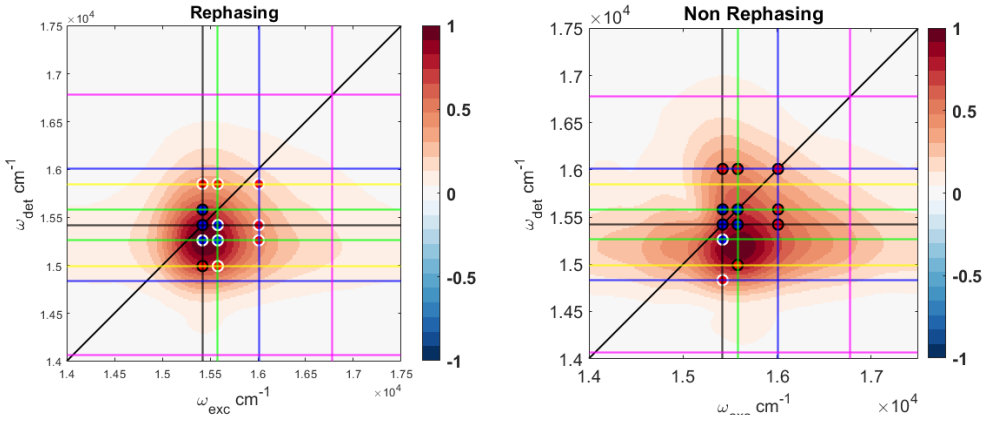

(a) 160 cm^{-1}

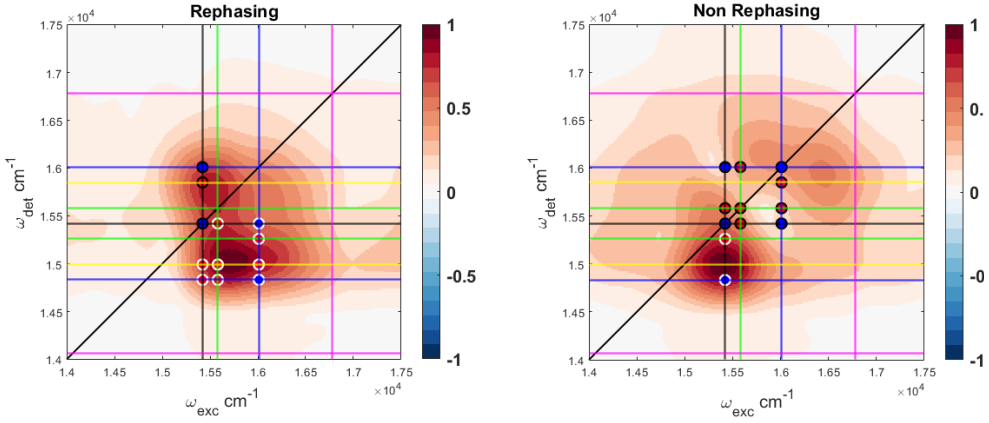

(b) 589 cm^{-1}

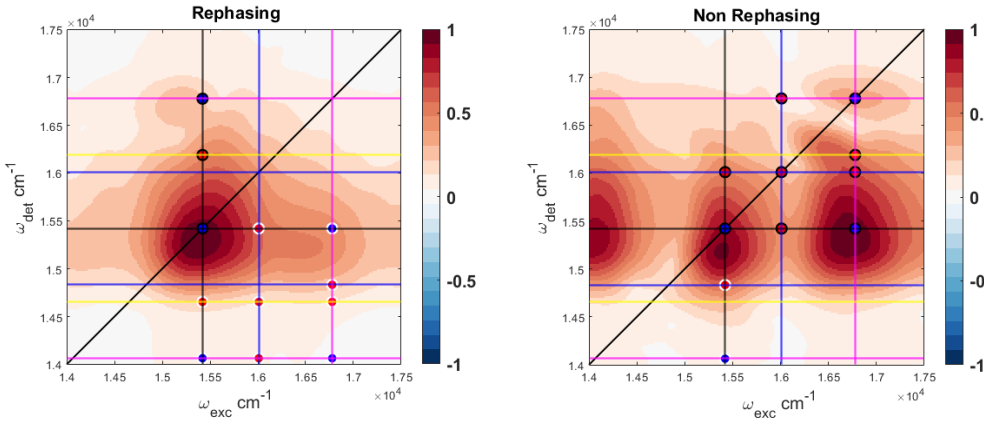

(c) 1357 cm^{-1}

Figure 4.11: 2D-CAS (absolute values) for each of the vibrational modes considered, for both R and NR signals; positive and negative frequency contributions are summed. Vertical and horizontal lines are traced at: ω_0 (black), $\omega_0 \pm$ 160 cm^{-1} (green), $\omega_0 \pm$ 589 cm^{-1} (blue), $\omega_0 \pm$ 1357 cm^{-1} (magenta). Yellow lines account for the mixed contributions: in (a) and (b) for $\omega_0 -$ 160 cm^{-1} + 589 cm^{-1}, in (c) $\omega_0 -$ 589 cm^{-1} + 1357 cm^{-1}. Blue circles represent the signal of the chair-like pattern, red circles represent the signal arising from the multi-mode vibrational coupling. White (black) outlines of the circles account for the positive (negative) frequency contributions.

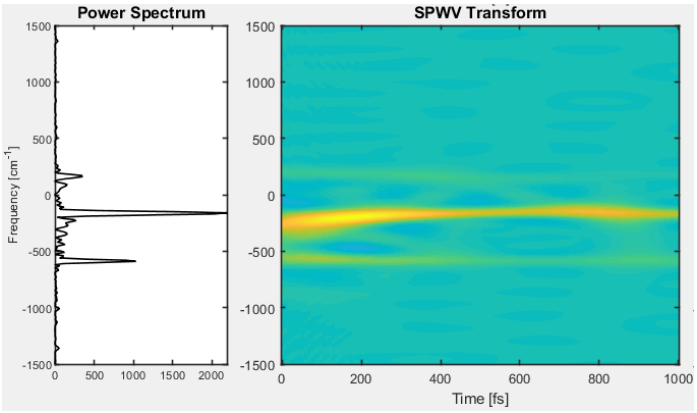

Figure 4.12: (Right) TFT analysis applied on the signal decay extracted at (15420, 14760) cm^{-1}. Among various TFT methods, here the smoothed-pseudo-Wigner-Ville (SPWV) transform is reported, as it is considered the most reliable in terms of signal clarity [85]. (Left) FSC (indicated here as "power spectrum") performed at the same coordinate, displayed for reference.

cisely as a coupling mode, exhibiting a significant change in its dynamic behavior approximately after 200 fs. This timing aligns closely with the 166 fs attributed to the crossing of the CI. Moreover, it is likely not a coincidence that its oscillation period (of about 200 fs) closely matches the 166 fs time constant of interest, which is highly encouraging as it indicates the involvement of the nuclear motions associated with this vibrational mode in the process itself [99]. A previous literature paper noted that the overlap of timescales presents a challenge in distinguishing between vibrational coherences that survive the CI crossing and those generated afterward [41]. While this issue is particularly relevant in the 1D pump-probe measurements used by the authors of the paper [41], it may not apply to the measurements in 2DES, where the intrinsic multidimensionality allows for better separation of signals. Nonetheless, additional analysis was performed to address this issue.

4.3.4 Beating Map

Further insights, particularly regarding the phase variation of the wavefunction, can be obtained using the so-called *beating maps*. Beating maps represent the coherent WP evolution resulting from the subtraction of the population kinetics. These maps are obtained by plotting the oscillating residue signal as a function of the detection frequency and t_2, following data integration over the excitation frequency. The result is shown in Figure (4.13).

The beating map displays nodes, each indicating a phase flip within the vibrational coherence. For an excited-state WP, a single node is expected to be localized around the maximum of the emission frequency. The node arises from the time evolution of the WP within the excited-state PES. As the WP traverses the potential well, it causes depletion or enhancement of the oscillating signal at different transition energies. Depending on which side of the PES the WP is positioned, the resulting signal can be slightly red- or blue-shifted relative to the emission frequency, with a phase flip occurring at the minimum. The red- and blue-shifted signals are temporally out of phase, thus

creating the node through interference [100, 101, 102]. While this phase flip is a universal signature of coherent vibrational oscillations, its microscopic origin is not always clear. A notable feature in this map is the observed frequency shifts of the node at population times $\gtrsim$ 160 fs [60].

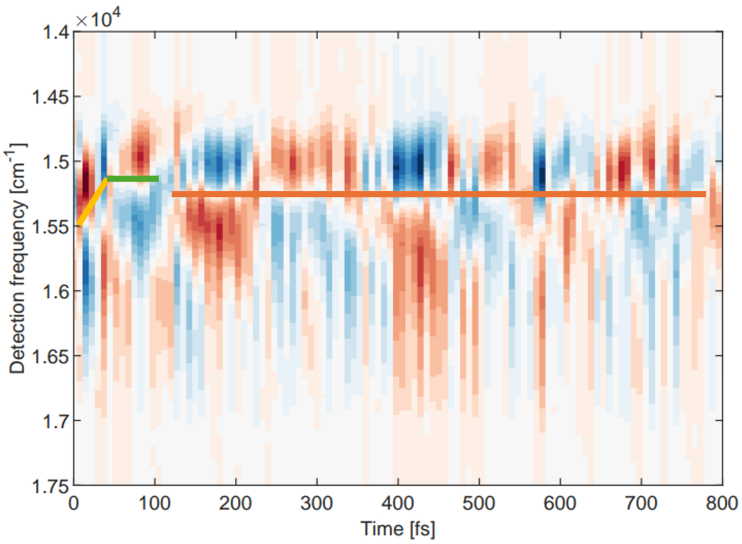

Figure 4.13: Beating map of SQ in acetonitrile. The yellow, green, and orange lines highlight the presence of the nodes and guide the eye in tracking their frequency shifts.

At early time delays, for $t_2 \lesssim 50$ fs, the node (pinpointed by the yellow line in Figure (4.13)) gradually shifts towards the maximum of the emission frequency (located at about 15100 cm^{-1} = 662 nm, as shown in Figure (2.7)), likely reflecting the relaxation from the vertically excited FC configuration [103]. Note that this timescale perfectly matches the first relaxation process identified in the population dynamics (Section 4.2, Figure (4.4a)) and supports the attribution of the shortest time constant to the electronic relaxation within the S_1 band driven by spectral diffusion and relaxation from the FC state. Then, for 50 fs $\lesssim t_2 \lesssim$ 150 fs, the node is found at the emission frequency (15100 cm^{-1}) as indicated by the green line. Finally, for $t_2 \gtrsim 165$ fs, it blue-shifts towards the absorption frequency (15400 cm^{-1}) (orange line). These results indicate that the WP oscillates on the excited state PES for the first ∼165 fs before transferring to the ground state, where it continues to oscillate for the rest of the observed time window. This behavior suggests that the WP passes through a CI in $\sim$ 165 fs. Notably, also this timescale aligns well with the findings of Section 4.2, reinforcing the interpretation that the second time constant (Figure (4.4b)) corresponds specifically to the crossing of a CI. As a general caution, it is important to note that the beating map shown in Figure (4.13) includes contributions from all frequencies. This may result in a partial blurring of the nodal lines and the associated phase shifts. We are currently conducting further analyses to separate the different contributions and obtain a distinct beating map for each relevant vibrational mode that is coupled to the electronic transition.

4.3.5 Final Remarks

Overall, the oscillating signal analysis indicates that the system undergoes nonradiative decay through a CI, with a characteristic time constant of 166 fs. Three primary vibrational modes are coupled to the electronic transition. They appear to be all anharmonically coupled, resulting in significant distortion in the central part of the molecule. This initial observation suggests that a plausible reaction coordinate involves the molecular distortion from the *p*-SQ to *d*-SQ conformation. Such a reaction coordinate implies a sloped potential energy landscape, as it involves only molecular twisting rather than an actual photoinduced reaction.
To describe the CI, we chose the minimal 2S2M framework. The relevant electronic states, S_0 and S_1, were already identified as involved in the CI dynamics through the 2D maps, but further details on the two vibrational modes constituting the branching space were required. The beating analysis, performed through various methodologies, suggested that the coupling and the tuning mode should be identified with the 160 cm^{-1} and the 589 cm^{-1}, respectively. These findings support both the appropriateness of the 2S2M model in this context and the roles of these modes in defining the CI. More in detail, the 160 cm^{-1} mode likely acts as the coupling mode, as its amplitude is strongly damped following the proposed crossing time [104, 105]. This damping arises from destructive interference at $Q_c = 0$, caused by a π phase shift acquired by the wavepacket along the two propagation pathways. Meanwhile, the 589 cm^{-1} mode presumably serves as the tuning mode, driving the structural distortions essential for the conformational change and maintaining a stable time evolution. The time behavior of this mode aligns with previous literature data, which indicates that tuning modes are generally unaffected by the CI crossing [105, 41]. The detection of a change in amplitude and frequency for the 160 cm^{-1} mode, as captured by the TFT analysis, offers preliminary indirect evidence of the geometric phase effect. However, the predicted time constant for the CI crossing is similar to the oscillation period of the coupling mode, which could result in potential misinterpretations of the TFT results. [41]. Thus, caution is necessary before considering this a definitive signature of the geometric phase effect. To address this limitation, we applied an alternative approach using the beating map, which showed node shifts around the anticipated CI crossing time. Initially, the node position indicated WP oscillation on the excited-state PES, later shifting to the ground-state surface approximately 160 fs after excitation. This timeframe aligns with the characteristic nonradiative decay period expected, confirming population transfer from S_1 to S_0 via CI crossing. This type of signature has been previously used as strong evidence for the Berry phase [60, 99].

4.4 Effect of the Environment and Substituents

This Section compares the results obtained for SQ in acetonitrile with the other datasets with the aim of capturing possible effects of the solvent and of the molecular substituents on the overall dynamics and particularly on the process involving the CI. We anticipate that, qualitatively, the 2D maps, 2D-DAS, and 2D-CAS are substantially similar to those found for SQ in acetonitrile. The only significant difference is in the time constants driving the relaxation dynamics.

SQ in Methanol. The global fitting output parameters for SQ in methanol are reported in Table (4.2).

Component index n	1	2	3	4	5	6	7
Frequency ω_n [cm^{-1}]	0	0	0	148	592	1056 (f)	1352
Time constant τ_n [fs]	10	193	>1000	500	1000	500(f)	>1000

Table 4.2: Output of the global fitting analysis including the oscillating components for SQ in methanol. The indication (f) stands for 'fixed' as the parameters attributed to the solvent contribution were set before performing the fitting.

The main difference among the time constants extracted for SQ in acetonitrile and methanol is in the second component, associated with the characteristic time required to cross the CI. The data suggest that SQ exhibits a slightly slower crossing rate in methanol than acetonitrile. Changes in the energy landscape caused by the solvent are typically attributed to either the dynamics of the solvent [106] or its stabilizing effects on molecular structures. Since solvent dynamics usually occur on a timescale that is much longer than the ultrafast processes being analyzed here, in the following discussion we will focus solely on the stabilizing effects.
The main solvent properties affecting molecular behavior include polarity, viscosity, and hydrogen-bonding capacity. Higher polarity can slow down the CI crossing by stabilizing the intermediate geometries and therefore increasing the energy barrier along the crossing pathway, making the CI less accessible [46]. Higher viscosity can similarly slow down the rate, primarily due to mechanical friction [47]. However, in our case, we do not anticipate a significant dependence on polarity and viscosity. This is mainly because the polarity and viscosity of acetonitrile and methanol are quite similar, and because experimental evidence shows that short-time dynamics, such as CI crossing, are only weakly affected by variations in polarity and viscosity [107, 108]. On the other hand, differences in the hydrogen-bonding network around the molecule have been found to appreciably affect the CI crossing rate [48]. This network is expected to differ in the acetonitrile and methanol, as the first is aprotic while the second is protic. Indeed, as discussed in Sections 2.1 and 2.2, methanol can act as a donor and acceptor towards the hydroxyl groups of the peripherical rings. In methanol, the formation of additional intermolecular H-bonds competes with the intramolecular H-bonds that stabilize the planar structure [65]. Consequently, the presence of the protic solvent would suggest a reduced stabilization of *p*-SQ, favoring molecular distortions and resulting in a lower energy barrier to access the CI. On the other hand, the more extended H-bonds network formed in methanol could lead to an overall more rigid system. In this scenario, a slowdown in the CI crossing is predicted compared to more 'flexible' environments [109]. Experimentally, we verified that, in methanol, the CI crossing rate is slightly slower than in acetonitrile, suggesting that the effect of a 'more rigid' environment may dominate. However, given the complexity of the intra- and inter-molecular interactions at play, further investigations from the experimental and theoretical perspectives are essential for a comprehensive understanding.

In the global fitting, a fixed vibrational mode with frequency $\sim$1050 cm^{-1} was included since it was associated with a solvent contribution [67]; it is clearly visible in FSC in Figure (4.14). This

mode can be easily attributed to the 1037 cm^{-1} Raman mode of methanol [110]. However, the presence of this spurious beating contribution did not compromise the analysis of the sample, as this mode does not overlap with any significant feature of the chromophores.

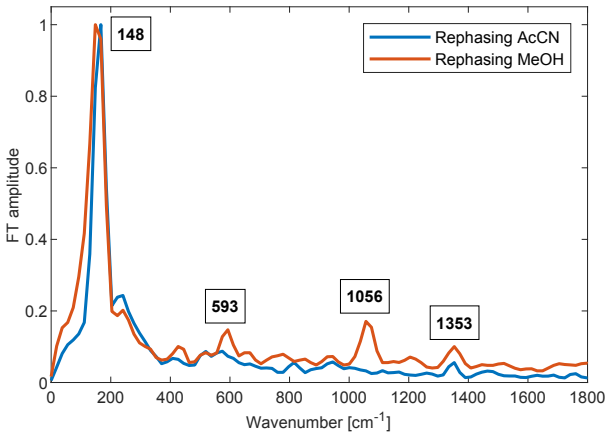

Figure 4.14: Comparison between the normalized FSC of the R signal for SQ in acetonitrile (blue) and methanol (orange). The intensity was normalized on the strongest peak for better comparison. Relevant peaks are labeled.

DBSQ in Acetonitrile. As for the previous sample, the output of the global fitting analysis is reported in Table (4.3).

Component index n	1	2	3	4	5	6
Frequency ω_n [cm^{-1}]	0	0	0	148	588	1519
Time constant τ_n [fs]	10	40	>1000	350	>1000	400

Table 4.3: Output of the global fitting analysis including the oscillating components for DBSQ in acetonitrile.

In this sample, the second time constant is significantly lower than in previous cases. If we assume that the photophysics of DBSQ is similar to that of SQ, it suggests that the crossing rate of DBSQ in acetonitrile is much faster than that of SQ. This difference can be tentatively justified considering the different N-substituents on each of the molecules' peripheral rings. Substituent effects can be categorized as 'inertial' or 'potential' [56]. Inertial substituents are assumed to be electronically inert chemical moieties, that serve to simply slow down (or speed up) specific vibrational motions by increasing (decreasing) the effective mass along a particular vibrational coordinate. Potential substituents, on the other hand, are considered to alter the underlying PESs, for example by tilting relevant pathways along the energy surfaces and therefore redirecting efficiently the wavepacket towards the CI, remarkably speeding up the rate of crossing [56]. Both inertial and potential effects influence the branching space around the CI. Moreover, the supposed coupling mode is related to the nuclear motion of substituents, explaining its significant weight in the overall CI dynamics [111]. N-diisobutyl is lighter and the inductive effect predominates, as for any simple

alkyl substituent. In contrast, N-dibenzyl is heavier and the electronic density can be redistributed through the mesomeric effect. When inertial and potential effects coexist and resonance effects are present, the potential effects generally dominate. Between inductive and mesomeric effects, the latter is more effective in directing nonadiabatic dynamics [112], by varying the slope of the pathway towards the CI and 'pushing' the WP along a particular coordinate [50]. With the distortion of the molecule due to the twisting, a charge imbalance is likely produced within the molecule. Thus, the N-dibenzyl substituent produces a greater overall stabilization along the reaction coordinate, significantly speeding up the CI crossing [49].

Concerning the oscillating part, the primary distinction between SQ and DBSQ lies in the higher-frequency coupled mode. As shown in Figure (4.15), DBSQ presents a 1519 cm^{-1} beating, which can be reasonably attributed to the $\sim$1505 cm^{-1} mode found in the calculations [65]. This vibration involves the motion of both the central core and the N-substituents, whereas the $\sim$1350 cm^{-1} mode in SQ corresponds solely to the breathing of the molecule's central core. This observation further suggests the significant impact of benzyl substituents on the overall dynamics, especially when compared to simpler alkyl substituents.

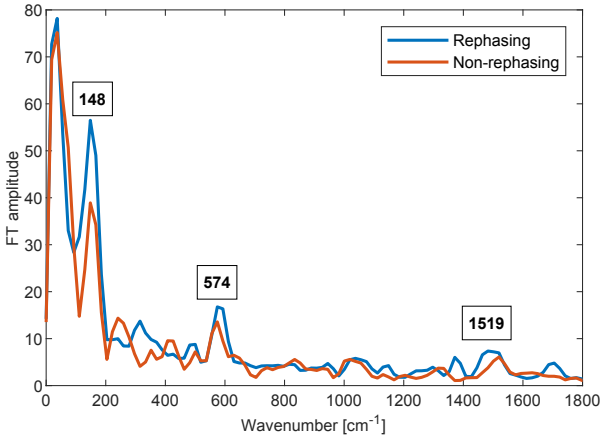

Figure 4.15: FSC for DBSQ in acetonitrile. Both R (blue) and NR (orange) contributions are reported and the main vibrational signals are labeled. The spectral region below 100 cm^{-1} is not considered due to the possible presence of artifacts.

Conclusions

This Thesis project investigated the ultrafast dynamics of three commercially available symmetrical squaraine dyes, aiming to explore relaxation pathways that may hinder charge separation and transport, crucial processes to guarantee a good efficiency of these dyes as sensitizers in DSSCs.
The initial characterization of the linear optical behavior of SQ, DSPQ, and DBSQ provided valuable insights into their excited-state properties, highlighting the significant role that specific vibrational modes play in the electronic transitions.
This preliminary information was crucial in the interpretation of the data collected by 2DES, providing a solid framework for understanding the photophysical and dynamical properties of this class of organic molecules. Through the application of several advanced data analysis methodologies, we successfully identified and characterized both population and coherence dynamics.

For all the studied samples, we found that the population relaxation is dominated by three distinct decaying components:

i. A fast-decaying component with a time constant of about 10 fs, linked with the initial ultrafast relaxation from the vertically excited FC state toward a relaxed configuration, and also accounting for spectral diffusion and pulse overlap effects.

ii. A second component with a time constant in the order of hundreds of fs, attributed to the crossing of a CI, which enables the ultrafast nonradiative decay of the excited-state population to the ground state. This second component demonstrates the greatest variability among the studied samples, as it is highly dependent on the type of substituents present and the nature of the solvent used.

iii. A final component with a much longer time constant ($\gg$ 1 ps), associated with the overall relaxation of the system back to the ground state.

The process most relevant to this Thesis is undoubtedly the second component. Several spectral features support its association with a CI, including the analysis of the oscillating components. The vibrational modes more strongly coupled with the electronic transition showed strongly anharmonic behavior and confirmed the presence of a CI with sloped topography, linked to the twisting of the molecule from a planar to a distorted conformation of the molecule. This nonadiabatic process involves the S_0 and S_1 electronic states, with the vibrational modes that define the branching space identified, for SQ, in the strongly coupled $\sim$160 cm^{-1} and $\sim$590 cm^{-1} modes. These modes are associated with the breathing of the donor moieties N-substituents and the twisting motion between the central rings.
From an application perspective, in DSSCs the presence of this nonradiative decay pathway could be highly detrimental due to its efficient deactivation of the excited state. However, in our samples, the deactivation via CI crossing accounted for only about 25% of the total decay, suggesting that while this pathway exists, it would not significantly compromise the dyes' effectiveness as sensitizers.

We also examined how environmental factors and dye substitution affect the CI crossing rate, finding that modifications to the dye's peripheral N-substituents produced the most significant changes. This underscores the critical role of substituents in modulating CI dynamics and suggests that lighter alkyl substituents could enhance DSSC performance.
Regarding the role of the solvent, we observed that while its effect was modest in our sample solutions, the presence of a rigid network of hydrogen bonds that restricts nuclear motion and molecular distortions could be a potential strategy. This approach may slow down the crossing of the CI and promote deactivation through more effective pathways.

Several exciting developments are envisioned for this project in the future. First, a more systematic characterization of squaraines with a wider range of substituents is needed to confirm the impact of molecular structure on the dynamics involved in the crossing of the CI. In this Thesis, the investigation of solvent effects was limited to two very similar solvents (in terms of polarity, viscosity, etc.) due to solubility and technical issues. However, exploring molecules with different functionalizations may broaden the range of solvents that could be studied, providing a clearer understanding of the role of the environment. This aspect is crucial when transitioning from a laboratory solution to a real material that will be incorporated into a working device. Another potential direction for future research would be to investigate squaraine aggregates, to determine how changes in electronic properties due to aggregation might influence vibronic coupling and the multi-mode interactions observed in monomeric forms.

In conclusion, the results presented in this Thesis represent a significant advancement in understanding the optical and electronic properties of this significant family of chromophores and shed light on the subtle effects dominating their relaxation dynamics.

References

[1] Paul T Anastas and John C Warner. *Green chemistry: theory and practice*. Oxford University Press, 2000.

[2] Chuanjiang Qin, Wai-Yeung Wong, and Liyuan Han. "Squaraine Dyes for Dye-Sensitized Solar Cells: Recent Advances and Future Challenges". In: *Chemistry–An Asian Journal* 8.8 (2013), pp. 1706–1719.

[3] Brian O'Regan and Michael Grätzel. "A low-cost, high-efficiency solar cell based on dye-sensitized colloidal TiO2 films". In: *Nature* 353.6346 (1991), pp. 737–740.

[4] Santhosh Sivaraj et al. "Dye-Sensitized Solar Cells". In: *Fundamentals of Solar Cell Design* (2021), pp. 137–167.

[5] Jiawei Gong, Jing Liang, and K Sumathy. "Review on dye-sensitized solar cells (DSSCs): Fundamental concepts and novel materials". In: *Renewable and Sustainable Energy Reviews* 16.8 (2012), pp. 5848–5860.

[6] Cameron Stanley, Ahmad Mojiri, and Gary Rosengarten. "Spectral light management for solar energy conversion systems". In: *Nanophotonics* 5.1 (2016), pp. 161–179.

[7] Sushil Khopkar and Ganapati Shankarling. "Synthesis, photophysical properties and applications of NIR absorbing unsymmetrical squaraines: A review". In: *Dyes and Pigments* 170 (2019), p. 107645.

[8] Jin He et al. "Squaraine dyes for photovoltaic and biomedical applications". In: *Advanced Functional Materials* 31.12 (2021), p. 2008201.

[9] Guo Chen et al. "Squaraine dyes for organic photovoltaic cells". In: *Journal of Materials Chemistry A* 3.28 (2015), pp. 14517–14534.

[10] Lei Hu, Zhengquan Yan, and Hongyao Xu. "Advances in synthesis and application of near-infrared absorbing squaraine dyes". In: *RSC advances* 3.21 (2013), pp. 7667–7676.

[11] Thomas AA Oliver. "Recent advances in multidimensional ultrafast spectroscopy". In: *Royal Society Open Science* 5.1 (2018), p. 171425.

[12] Kristin LM Lewis and Jennifer P Ogilvie. "Probing photosynthetic energy and charge transfer with two-dimensional electronic spectroscopy". In: *The journal of physical chemistry letters* 3.4 (2012), pp. 503–510.

[13] Vladimir I Novoderezhkin et al. "Exciton-vibrational resonance and dynamics of charge separation in the photosystem II reaction center". In: *Physical Chemistry Chemical Physics* 19.7 (2017), pp. 5195–5208.

[14] Elisa Fresch et al. "Two-dimensional electronic spectroscopy". In: *Nature Reviews Methods Primers* 3.1 (2023), p. 84.

[15] Shaul Mukamel. *Principles of Nonlinear Optical Spectroscopy*. 1995.

[16] William W Parson. *Modern Optical Spectroscopy*. Vol. 2. Springer, 2007.

[17] Eugene Hecht. *Optics, 5e*. Pearson Education India, 2002.

[18] R.W Boyd. *Nonlinear Optics*. Elsevier, 2003.

[19] Minhaeng Cho. *Two-dimensional Optical Spectroscopy*. CRC press, 2009.

[20] Agata M Brańczyk, Daniel B Turner, and Gregory D Scholes. "Crossing disciplines-A view on two-dimensional optical spectroscopy". In: *Annalen der Physik* 526.1-2 (2014), pp. 31–49.

[21] Andrei Tokmakoff. *Nonlinear and Two-Dimensional Spectroscopy*. 2014. URL: `https://tdqms.uchicago.edu/`.

[22] Elisabetta Collini. "2D Electronic Spectroscopic Techniques for Quantum Technology Applications". In: *The Journal of Physical Chemistry C* 125.24 (2021), pp. 13096–13108.

[23] Kenji Ohmori. "Wave-packet and coherent control dynamics". In: *Annual Review of Physical Chemistry* 60 (2009), pp. 487–511.

[24] Vytautas Butkus et al. "Vibrational vs. electronic coherences in 2D spectrum of molecular systems". In: *Chemical Physics Letters* 545 (2012), pp. 40–43.

[25] Michael Kasha, Henry R Rawls, and M Ashraf El-Bayoumi. "The exciton model in molecular spectroscopy". In: *Pure and Applied Chemistry VIIIth* 11.3-4 (1965), pp. 371–392.

[26] Daniel B Turner et al. "Comparison of electronic and vibrational coherence measured by two-dimensional electronic spectroscopy". In: *The Journal of Physical Chemistry Letters* 2.15 (2011), pp. 1904–1911.

[27] Camille A Farfan and Daniel B Turner. "Interference among multiple vibronic modes in two-dimensional electronic spectroscopy". In: *Mathematics* 8.2 (2020), p. 157.

[28] Katherine A Kitney-Hayes et al. "Two-dimensional Fourier transform electronic spectroscopy at a conical intersection". In: *The Journal of Chemical Physics* 140.12 (2014).

[29] Tessa R Calhoun et al. "The separation of overlapping transitions in β-carotene with broadband 2D electronic spectroscopy". In: *Chemical Physics Letters* 523 (2012), pp. 1–5.

[30] Max Born and Robert Oppenheimer. "On the quantum theory of molecules". In: *Quantum Chemistry: Classic Scientific Papers*. World Scientific, 2000, pp. 1–24.

[31] Spiridoula Matsika. "Conical intersections in molecular systems". In: *Reviews in Computational Chemistry* 23 (2007), p. 83.

[32] Wolfgang Domcke, Horst Koppel, and David R Yarkony. *Conical intersections: electronic structure, dynamics & spectroscopy*. Vol. 15. World Scientific, 2004.

[33] David R Yarkony. "Conical intersections: The new conventional wisdom". In: *The Journal of Physical Chemistry A* 105.26 (2001), pp. 6277–6293.

[34] David R Yarkony. "Conical intersections: Diabolical and often misunderstood". In: *Accounts of Chemical Research* 31.8 (1998), pp. 511–518.

[35] Gloria Olaso-González, Manuela Merchán, and Luis Serrano-Andrés. "Ultrafast electron transfer in photosynthesis: Reduced pheophytin and quinone interaction mediated by conical intersections". In: *The Journal of Physical Chemistry B* 110.48 (2006), pp. 24734–24739.

[36] Dario Polli et al. “Conical intersection dynamics of the primary photoisomerization event in vision”. In: *Nature* 467.7314 (2010), pp. 440–443.

[37] Carlos E Crespo-Hernández et al. “Ultrafast excited-state dynamics in nucleic acids”. In: *Chemical reviews* 104.4 (2004), pp. 1977–2020.

[38] Rocío Borrego-Varillas et al. “Tracking excited state decay mechanisms of pyrimidine nucleosides in real time”. In: *Nature Communications* 12.1 (2021), p. 7285.

[39] Marcos Dantus and Ahmed Zewail. *Introduction: femtochemistry*. 2004.

[40] Ahmed M El-Zohry, Daniel Roca-Sanjuan, and Burkhard Zietz. “Ultrafast twisting of the indoline donor unit utilized in solar cell dyes: experimental and theoretical studies”. In: *The Journal of Physical Chemistry C* 119.5 (2015), pp. 2249–2259.

[41] Matz Liebel, Christoph Schnedermann, and Philipp Kukura. “Vibrationally coherent crossing and coupling of electronic states during internal conversion in β-carotene”. In: *Physical Review Letters* 112.19 (2014), p. 198302.

[42] Wolfgang Domcke, David Yarkony, and Horst Köppel. *Conical intersections: theory, computation and experiment*. Vol. 17. World Scientific, 2011.

[43] Gregory J Atchity, Sotirios S Xantheas, and Klaus Ruedenberg. “Potential energy surfaces near intersections”. In: *The Journal of Chemical Physics* 95.3 (1991), pp. 1862–1876.

[44] Giulio Cerullo and Marco Garavelli. “A novel spectroscopic window on conical intersections in biomolecules”. In: *Proceedings of the National Academy of Sciences* 117.43 (2020), pp. 26553–26555.

[45] Spiridoula Matsika and Pascal Krause. “Nonadiabatic events and conical intersections”. In: *Annual Review of Physical Chemistry* 62.1 (2011), pp. 621–643.

[46] Anat Kahan et al. “Solvent tuning of a conical intersection: direct experimental verification of a theoretical prediction”. In: *The Journal of Physical Chemistry A* 115.40 (2011), pp. 10854–10861.

[47] Eric C Wu et al. “Two-dimensional electronic-vibrational spectroscopic study of conical intersection dynamics: an experimental and electronic structure study”. In: *Physical Chemistry Chemical Physics* 21.26 (2019), pp. 14153–14163.

[48] Teng-Shuo Zhang et al. “Hydrogen-bonding interaction regulates photoisomerization of a single-bond-rotation locked photoactive yellow protein chromophore in protein”. In: *The Journal of Physical Chemistry Letters* 11.7 (2020), pp. 2470–2476.

[49] Ryan J MacDonell et al. “Excited state dynamics of acrylonitrile: Substituent effects at conical intersections interrogated via time-resolved photoelectron spectroscopy and ab initio simulation”. In: *The Journal of Chemical Physics* 145.11 (2016).

[50] Ryan J MacDonell and Michael S Schuurman. “Substituent effects on the nonadiabatic dynamics of ethylene: π-donors and π-acceptors”. In: *Chemical Physics* 515 (2018), pp. 360–368.

[51] Benjamin G Levine and Todd J Martínez. “Isomerization through conical intersections”. In: *Annu. Rev. Phys. Chem.* 58.1 (2007), pp. 613–634.

[52] Remedios González-Luque et al. “Computational evidence in favor of a two-state, two-mode model of the retinal chromophore photoisomerization”. In: *Proceedings of the National Academy of Sciences* 97.17 (2000), pp. 9379–9384.

[53] Hong-Guang Duan and Michael Thorwart. “Quantum mechanical wave packet dynamics at a conical intersection with strong vibrational dissipation”. In: *The Journal of Physical Chemistry Letters* 7.3 (2016), pp. 382–386.

[54] Alessandro Ferretti, Alessandro Lami, and Giovanni Villani. “A model study of the wavepacket dynamics around a Jahn–Teller conical intersection in a symmetric charge-transfer system”. In: *Chemical Physics* 259.2-3 (2000), pp. 201–210.

[55] Yorrick Boeije and Massimo Olivucci. “From a one-mode to a multi-mode understanding of conical intersection mediated ultrafast organic photochemical reactions”. In: *Chemical Society Reviews* 52.8 (2023), pp. 2643–2687.

[56] Michael S Schuurman and Albert Stolow. “Dynamics at conical intersections”. In: *Annual review of physical chemistry* 69.1 (2018), pp. 427–450.

[57] Jindřich Krčmář et al. “Signatures of conical intersections in two-dimensional electronic spectra”. In: *Journal of Physics B: Atomic, Molecular and Optical Physics* 47.12 (2014), p. 124019.

[58] Gerhard Herzberg and H Christopher Longuet-Higgins. “Intersection of potential energy surfaces in polyatomic molecules”. In: *Discussions of the Faraday Society* 35 (1963), pp. 77–82.

[59] Michael Victor Berry. “Quantal phase factors accompanying adiabatic changes”. In: *Proceedings of the Royal Society of London. A. Mathematical and Physical Sciences* 392.1802 (1984), pp. 45–57.

[60] Johanna Brazard et al. “Experimental detection of branching at a conical intersection in a highly fluorescent molecule”. In: *The Journal of Physical Chemistry Letters* 7.1 (2016), pp. 14–19.

[61] Hong-Guang Duan, RJ Dwayne Miller, and Michael Thorwart. “Impact of vibrational coherence on the quantum yield at a conical intersection”. In: *The Journal of Physical Chemistry Letters* 7.17 (2016), pp. 3491–3496.

[62] Fabienne Meyers et al. “Electronic structure and linear and nonlinear optical properties of symmetrical and unsymmetrical squaraine dyes”. In: *Chemistry–A European Journal* 3.4 (1997), pp. 530–537.

[63] Daniel Timmer et al. “Charge delocalization and vibronic couplings in quadrupolar squaraine dyes”. In: *Journal of the American Chemical Society* 144.41 (2022), pp. 19150–19162.

[64] Alagesan Subramanian and Hong-Wen Wang. “Effect of hydroxyl group attachment on TiO2 films for dye-sensitized solar cells”. In: *Applied Surface Science* 258.20 (2012), pp. 7833–7838.

[65] Edoardo Buttarazzi et al. “Conformational and environmental effects on the electronic and vibrational properties of dyes for solar cell devices”. In: *The Journal of Chemical Physics* 160.20 (2024).

[66] Peng Zhao et al. “Temporal and polarization dependence of the nonlinear optical response of solvents”. In: *Optica* 5.5 (2018), pp. 583–594.

[67] Karel Bouda et al. “Solvent signals in two-dimensional electronic spectroscopy”. In: *AIP Advances* 12.11 (2022).

[68] Sivaramapanicker Sreejith et al. “Squaraine dyes: a mine of molecular materials”. In: *Journal of Materials Chemistry* 18.3 (2008), pp. 264–274.

[69] Andrea M Della Pelle et al. “Effect of substituents on optical properties and charge-carrier polarity of squaraine dyes”. In: *The Journal of Physical Chemistry C* 118.4 (2014), pp. 1793–1799.

[70] Luca Beverina and Patrizio Salice. “Squaraine compounds: Tailored design and synthesis towards a variety of material science applications”. In: *European journal of organic chemistry* 2010.7 (2010), pp. 1207–1225.

[71] Carlo Toro et al. “Linear and nonlinear optical characterizations of a monomeric symmetric squaraine-based dye in solution”. In: *The Journal of Chemical Physics* 130.21 (2009).

[72] Raffaele Borrelli, Silvano Ellena, and Claudia Barolo. “Theoretical and experimental determination of the absorption and emission spectra of a prototypical indolenine-based squaraine dye”. In: *Physical Chemistry Chemical Physics* 16.6 (2014), pp. 2390–2398.

[73] Wolfgang Becker et al. “Advanced time-correlated single photon counting techniques for spectroscopy and imaging in biomedical systems”. In: *Commercial and Biomedical Applications of Ultrafast Lasers IV*. Vol. 5340. SPIE. 2004, pp. 104–112.

[74] JR Lakowicz. “Principles of fluorescence spectroscopy”. In: *University of Maryland School of Medicine Baltimore* 132 (2006).

[75] Kock-Yee Law, F Court Bailey, and Lynn J Bluett. “Squaraine chemistry. On the anomalous mass spectra of bis (4-dimethylaminophenyl) squaraine and its derivatives”. In: *Canadian Journal of Chemistry* 64.8 (1986), pp. 1607–1619.

[76] Andrius Gelzinis et al. “Two-dimensional spectroscopy for non-specialists”. In: *Biochimica et Biophysica Acta (BBA)-Bioenergetics* 1860.4 (2019), pp. 271–285.

[77] Luca Bolzonello et al. “Versatile setup for high-quality rephasing, non-rephasing, and double quantum 2D electronic spectroscopy”. In: *JOSA B* 34.6 (2017), pp. 1223–1233.

[78] Franklin D Fuller and Jennifer P Ogilvie. “Experimental implementations of two-dimensional Fourier transform electronic spectroscopy”. In: *Annual Review of Physical Chemistry* 66.1 (2015), pp. 667–690.

[79] David M Jonas. “Two-dimensional femtosecond spectroscopy”. In: *Annual Review of Physical Chemistry* 54.1 (2003), pp. 425–463.

[80] John D Hybl et al. “Two-dimensional electronic spectroscopy”. In: *Chemical Physics Letters* 297.3-4 (1998), pp. 307–313.

[81] Steven T Cundiff. “Optical three-dimensional coherent spectroscopy”. In: *Physical Chemistry Chemical Physics* 16.18 (2014), pp. 8193–8200.

[82] Hebin Li et al. “Unraveling quantum pathways using optical 3D Fourier-transform spectroscopy”. In: *Nature Communications* 4.1 (2013), pp. 1–9.

[83] Andrea Volpato et al. “Global analysis of coherence and population dynamics in 2D electronic spectroscopy”. In: *Optics Express* 24.21 (2016), pp. 24773–24785.

[84] Elena Meneghin, Danilo Pedron, and Elisabetta Collini. “Raman and 2D electronic spectroscopies: A fruitful alliance for the investigation of ground and excited state vibrations in chlorophyll a”. In: *Chemical Physics* 514 (2018), pp. 132–140.

[85] Andrea Volpato and Elisabetta Collini. “Time-frequency methods for coherent spectroscopy”. In: *Optics Express* 23.15 (2015), pp. 20040–20050.

[86] Duc Viet Le et al. “Characterization of the ultrafast spectral diffusion and vibronic coherence of TIPS-pentacene using 2D electronic spectroscopy”. In: *The Journal of Chemical Physics* 155.1 (2021).

[87] Mattia Russo et al. “Dephasing processes in the molecular dye lumogen-f orange characterized by two-dimensional electronic spectroscopy”. In: *Molecules* 27.20 (2022), p. 7095.

[88] Tatsuya Yoshida and Kazuya Watanabe. “Spectral Diffusion of Excitons in 3, 4, 9, 10-Perylenetetracarboxylic-diimide (PTCDI) Thin Films”. In: *The Journal of Physical Chemistry B* 125.32 (2021), pp. 9350–9356.

[89] Elena Meneghin et al. “Mechanistic insight into internal conversion process within Q-bands of chlorophyll a”. In: *Scientific Reports* 7.1 (2017), p. 11389.

[90] Luca Bolzonello et al. “Two-dimensional electronic spectroscopy reveals dynamics and mechanisms of solvent-driven inertial relaxation in polar BODIPY dyes”. In: *The Journal of Physical Chemistry Letters* 9.5 (2018), pp. 1079–1085.

[91] Francesca Terenziani et al. “Charge instability in quadrupolar chromophores: Symmetry breaking and solvatochromism”. In: *Journal of the American Chemical Society* 128.49 (2006), pp. 15742–15755.

[92] Antonio Inchingolo. “Coherent Dynamics in the Ultrafast Relaxation of red absorbing squaraine Dyes: 2D Electronic Spectroscopic Characterization”. MA thesis. Università degli Studi di Padova, 2022/2023.

[93] Minhaeng Cho. “Coherent two-dimensional optical spectroscopy”. In: *Chemical Reviews* 108.4 (2008), pp. 1331–1418.

[94] Andrew F Fidler and Gregory S Engel. “Nonlinear spectroscopic theory of displaced harmonic oscillators with differing curvatures: A correlation function approach”. In: *The Journal of Physical Chemistry A* 117.39 (2013), pp. 9444–9453.

[95] Ruidan Zhu et al. “Electronic state-resolved multimode-coupled vibrational wavepackets in oxazine 720 by two-dimensional electronic spectroscopy”. In: *The Journal of Physical Chemistry A* 124.45 (2020), pp. 9333–9342.

[96] Shuai Yue et al. “Coupling of multi-vibrational modes in bacteriochlorophyll a in solution observed with 2D electronic spectroscopy”. In: *Chemical Physics Letters* 683 (2017), pp. 591–597.

[97] Veronica R Policht, Andrew Niedringhaus, and Jennifer P Ogilvie. “Characterization of vibrational coherence in monomeric bacteriochlorophyll a by two-dimensional electronic spectroscopy”. In: *The Journal of Physical Chemistry Letters* 9.22 (2018), pp. 6631–6637.

[98] Franklin D Fuller et al. “Vibronic coherence in oxygenic photosynthesis”. In: *Nature chemistry* 6.8 (2014), pp. 706–711.

[99] Qing Wang et al. “Vibrationally coherent photochemistry in the femtosecond primary event of vision”. In: *Science* 266.5184 (1994), pp. 422–424.

[100] Jeffrey A Cina et al. “Ultrafast transient absorption revisited: Phase-flips, spectral fingers, and other dynamical features”. In: *The Journal of Chemical Physics* 144.17 (2016).

[101] Paul C Arpin and Daniel B Turner. “Signatures of vibrational and electronic quantum beats in femtosecond coherence spectra”. In: *The Journal of Physical Chemistry A* 125.12 (2021), pp. 2425–2435.

[102] Colin Fitzpatrick, Johanan H Odhner, and Robert J Levis. “Spectral signatures of ground- and excited-state wavepacket interference after impulsive excitation”. In: *The Journal of Physical Chemistry A* 124.34 (2020), pp. 6856–6866.

[103] Scott D McClure et al. “Coherent oscillations in the PC577 cryptophyte antenna occur in the excited electronic state”. In: *The Journal of Physical Chemistry B* 118.5 (2014), pp. 1296–1308.

[104] Christoph Schnedermann, Matz Liebel, and Philipp Kukura. “Mode-specificity of vibrationally coherent internal conversion in rhodopsin during the primary visual event”. In: *Journal of the American Chemical Society* 137.8 (2015), pp. 2886–2891.

[105] Da-Long Qi et al. “Tracking an electronic wave packet in the vicinity of a conical intersection”. In: *The Journal of Chemical Physics* 147.7 (2017).

[106] Riccardo Spezia, Irene Burghardt, and James T Hynes. “Conical intersections in solution: non-equilibrium versus equilibrium solvation”. In: *Molecular Physics* 104.5-7 (2006), pp. 903–914.

[107] L Nikowa et al. “Viscosity and solvent dependence of low-barrier processes: Photoisomerization of cis-stilbene in compressed liquid solvents”. In: *The Journal of Chemical Physics* 97.7 (1992), pp. 4827–4835.

[108] Irene Burghardt and James T Hynes. “Excited-state charge transfer at a conical intersection: Effects of an environment”. In: *The Journal of Physical Chemistry A* 110.40 (2006), pp. 11411–11423.

[109] Elisa Pieri et al. “Conical intersection accessibility dictates brightness in red fluorescent proteins”. In: *Journal of the American Chemical Society* 146.26 (2024), pp. 17646–17658.

[110] RE Hester and RA Plane. “Raman spectra of methanol solutions—I: Saturated solutions of some electrolytes”. In: *Spectrochimica Acta Part A: Molecular Spectroscopy* 23.8 (1967), pp. 2289–2296.

[111] Simon P Neville et al. “Substituent effects on dynamics at conical intersections: Allene and methyl allenes”. In: *The Journal of Chemical Physics* 144.1 (2016).

[112] Artur Nenov and Regina de Vivie-Riedle. “Geometrical and substituent effects in conical intersections: Linking chemical structure and photoreactivity in polyenes”. In: *The Journal of Chemical Physics* 135.3 (2011).

Ringraziamenti

Desidero esprimere la mia più profonda gratitudine alla prof.ssa Collini per la sua costante e paziente guida durante il percorso di ricerca. La sua precisione, cura e entusiasmo sono stati per me una fonte di grande ispirazione, infondendomi sicurezza e motivandomi a proseguire con determinazione il mio progetto.
Un sentito ringraziamento va al prof. Petrone e al suo gruppo per la loro fondamentale collaborazione e per aver fornito dati essenziali per lo sviluppo di questo lavoro.
Infine, desidero ringraziare di cuore Federico, Elisa e Francesco per il loro prezioso supporto e per i numerosi consigli che hanno arricchito il mio percorso. La loro disponibilità e il tempo inestimabile che mi hanno dedicato sono stati indispensabili per superare le difficoltà incontrate lungo il cammino.

A tutti loro, la mia più sincera riconoscenza.